Preface

Master thesis in Marine Technology (TMR4930), spring semester 2024.

I express my sincere gratitude to Prof. Lars Erik Holmedal, Cai Tian and Jianxun Zhu at the Department of Marine Technology, NTNU for the great assistance and support during both the fall semester of 2023 and the spring semester of 2024 while working on the very interesting topic of this thesis. Their expertise and assistance has contributed to my knowledge and understanding, as well as helped my motivation during the process. I would like to thank Cai Tian for the thorough assistance and guidance in performing simulations with the numerical code MGLET, due to his expertise. Computing resources were granted by the Norwegian Research Council (Program for Supercomputing) under project NN9352K.

Markus Knutsen, Trondheim 06.06.2024

Abstract

Uniform cylinders are commonly encountered in numerous engineering applications, and the flow past uniform cylinders is critical to the structural loading (the drag and lift). This thesis investigates the dual step cylinder, which is a uniform cylinder of diameter d (referred to as the small cylinder) that has a large cylinder of diameter D and length L on the mid span, with $d < D$. The vortex dynamics and the structural loading in a dual step cylinder flow are investigated numerically at Reynolds number Re_D=150 for diameter ratio $D/d = 1.33$ and aspect ratios $L/D = 1, 3$ and 5. The vortex structures are investigated and the frequency content of the vortex shedding along the span of the dual step cylinder is analyzed. It is found that for $L/D = 1$ and 5, the small cylinder vortices shed in phase with each other, whereas for $L/D = 3$, the small cylinder vortices shed completely (180°) out of phase. Due to the out-of-phase shedding of the dual step cylinder with $L/D = 3$, the lift forces begin to cancel each other out, resulting in a 94% reduction in the lift force compared to the structural load of a uniform cylinder. It is found an increasing phase-corrected lift force with increasing L/D. It is not found any reduction in the drag force of a dual step cylinder compared to the structural loading of a uniform cylinder, for any aspect ratios.

Rette, sirkulære sylindere er vanlige i mange tekniske konstruksjoner, og strømningsforholdene rundt rette sylindere er kritiske for kreftene som utøves på konstruksjonene (drag- og løftekefter). Denne oppgaven fokuserer på dobbeltsteg sylinderen, som er en rett sylinder med diameter d (referert til som den lille sylinderen) og som har en stor sylinder med diameter D og lengde L på midten, hvorav $d < D$. Numeriske undersøkelser av strømningen rundt dobbeltsteg sylindre med diameterforhold $D/d = 1.33$ og sideforhold $L/D = 1, 3$ og 5 ved Reynolds-tall $Re_D = 150$ er gjennomført. Virvelstrukturene og frekvensinnholdet i virvelavløsningen langs hele spennet til dobbeltsteg sylindrene er analysert. Det kommer frem at for $L/D = 1$ og 5 så er virvelavløsningen på de små sylindrene i fase med hverandre. For $L/D = 3$, så er virvelavløsningen på de små sylindrene i motfase (faseforskjøvet 180°), noe som gjør at løftekreftene begynne å kansellere hverandre. Dette resulterer i en 94% reduksjon i løftekraft for dobbeltsteg sylinderen med $L/D = 3$ sammenlignet med løftekreftene som blir utøvd på en rett sylinder. Det kommer frem at den fasekorrigerte løftekraften stiger med et stigende sideforhold L/D. Det ble ikke funnet reduksjon i dragkrefter for noen av sideforholdene, sammenlignet med dragkreftene som blir utøvd på en rett sylinder.

Contents

Preface **i**

Abstract **iii**

Contents **v**

List of Figures **vii**

List of Tables **ix**

1 Introduction **1**

2 Governing equations, computational method and convergence study **11**
2.1 Computational method 11
2.2 Grid convergence 14
2.3 Spanwise length convergence 16
2.4 Simulation overview 17

3 Results and discussion **19**
3.1 Comparisons with the results by McClure et al. (2015) 19
3.2 Features of the wake flow with varying aspect ratio 26
3.3 Effects on structural loading with varying aspect ratio 33

4 Summary and conclusion **39**
4.1 Further work 40

References **41**

List of Figures

1.1 Illustration of four different step cylinder configurations 2
1.2 Illustration of two-dimensional Karman vortex shedding 2
1.3 Illustration of flow regimes around a circular cylinder 3
1.4 Illustration of the S-, N- and L-cell in the wake behind a single step cylinder 4
1.5 Experimental visualization of the S-, N- and L-cell in the wake behind a single step cylinder 4
1.6 Experimental visualization of the flow past a dual step cylinder 5
1.7 Experimental visualization of the flow past a multi step cylinder 5
1.8 Illustration of flat sinusoidal cylinder from Bearman and Owen (1998) 7
1.9 Illustration of sinusoidal cylinder from Lee and Nguyen (2007) 7
1.10 Illustration of cylinder with hemispherical bumps from Owen et al. (2001) 8
1.11 Illustration of twisted cylinder from Yoon et al. (2019) 8
1.12 Illustration of circular cylinder with cylindrical rings along its span from Nakamura and Igarashi (2008) 8

2.1.1 Illustration of the multi-level grids in the xz-plane 12
2.1.2 Illustration of the multi-level grids in the xy-plane 13
2.2.1 Distribution of the time-averaged streamwise velocity $\overline{u/U}$ in the grid convergence study 15
2.2.2 Distribution of the mean drag coefficient $\overline{C_D^*}$ in the grid convergence study 15
2.2.3 Distribution of the rms lift coefficient C_{LRMS}^* in the grid convergence study 15
2.3.1 Distribution of the mean drag coefficient $\overline{C_D^*}$ in the spanwise length convergence study 16
2.3.2 Distribution of the rms lift coefficient C_{LRMS}^* in the spanwise length convergence study 16
2.4.1 Illustration of the geometrical configuration of cases L1, L3 and L5 17

3.1.1 Vortex structures from McClure et al. (2015) 20
3.1.2 Vortex structure for case Fine-B 20
3.1.3 Spanwise vorticity contours in the wake behind the large cylinder, from McClure et al. (2015) 21
3.1.4 Spanwise vorticity contours in the wake behind the large cylinder for case Fine-B 21
3.1.5 Recirculation length from McClure et al. (2015) 23
3.1.6 The recirculation length in the spanwise length convergence study 23
3.1.7 Lift coefficient time series $C_L(t)$ of a uniform cylinder at $Re = 75$ 24
3.2.1 3D frequency spectrum plot of the streamwise velocity fluctuations for case L1, L3 and L5 26
3.2.2 Vortex structures for the beat frequency $f_B D/U$ of case L1 27
3.2.3 Vortex structures for the beat frequency $f_B D/U$ of case L3 28
3.2.4 Vortex structures for case L1 and L5 29
3.2.5 Vortex structures for case L3 31
3.3.1 Time series of the lift- and drag force for cases L1, L3 and L5 33
3.3.2 Frequency content of the time history of the drag force F_D for case L5 34
3.3.3 Time series of the lift force F_L for case L3 at $400 \leq tU/D \leq 800$ 34
3.3.4 Force coefficients of cases L1, L3 and L5 compared to force coefficients of a uniform cylinder 36

List of Tables

2.1.1 Convergence study simulation information table 13
2.4.1 Aspect ratio study simulation information table 17

3.1.1 Tabulated differences between case Fine-B and McClure et al. (2015) 24

CHAPTER 1

Introduction

The flow past uniform cylindrical structures is commonly encountered in engineering applications such as industrial chimneys, pipelines and other cylindrical mechanical components or structures. As the flow is critical to the forces on the cylinder, the flow past a uniform cylinder has been the subject of a significant number of research papers over the years. The flow past different step cylinder configurations have recently been gaining attention due to their different applications such as in SPAR platforms, steel lazy wave risers (Yin et al., 2020) and the outer wall of TV-towers. Compared to the uniform cylinder, a step cylinder has one or more step-changes in diameter, which causes complex flow interactions in the wake behind the step(s). There are multiple different step cylinder geometries that have been studied, such as a single step cylinder (Tian et al., 2023b), dual step cylinder (McClure et al., 2015), multi step cylinder (Wu et al., 2020) and I step cylinder (Tian et al., 2022). Figure 1.1(a), (b), (c) and (d) illustrates the single step-, dual step-, multi step- and I step cylinder configuration respectively.

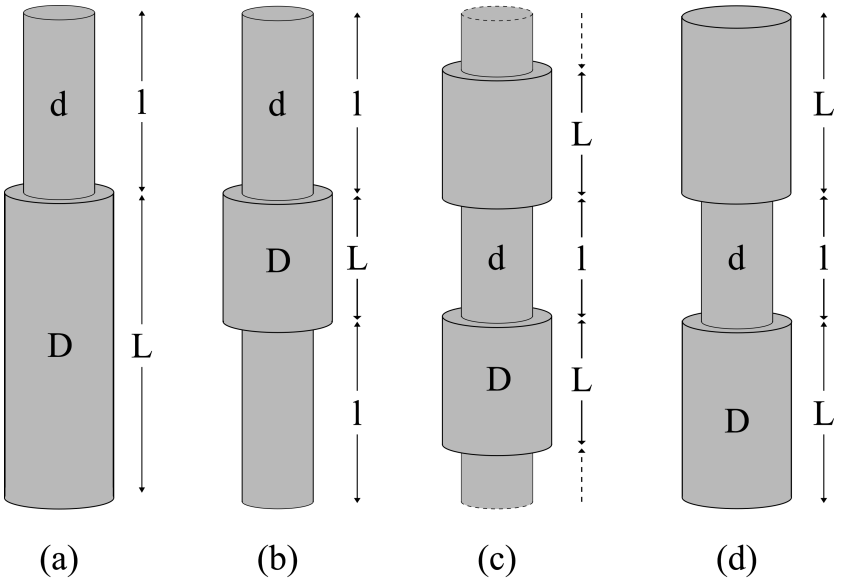

Figure 1.1: Illustration of four different step cylinder configurations. For all configurations, L and D represents the large cylinder length and diameter, and l and d represents the small cylinder length and diameter. Configuration (a) illustrates the single step cylinder, (b) illustrates the dual step cylinder, (c) illustrates the multi step cylinder and (d) illustrates the I step cylinder.

The Reynolds number Re governs the behaviour of the wake of the cylinder and is defined as $Re = DU/\nu$, where D is the diameter of the cylinder, U is the incoming flow velocity and ν is the kinematic viscosity of the fluid. The flow undergoes significant change as Re is increased, and the multiple different flow regimes that are discernible from the flow based on Re are illustrated in figure 1.3 from Sumer and Fredsøe (2006). For $Re < 49$, there are only two steady recirculating vortices in the wake of the cylinder (C. H. K. Williamson, 1996). When $Re > 50$ the wake develops instabilities and a periodic two-dimensional vortex shedding commences, as illustrated in figure 1.2 from C. H. K. Williamson (1996).

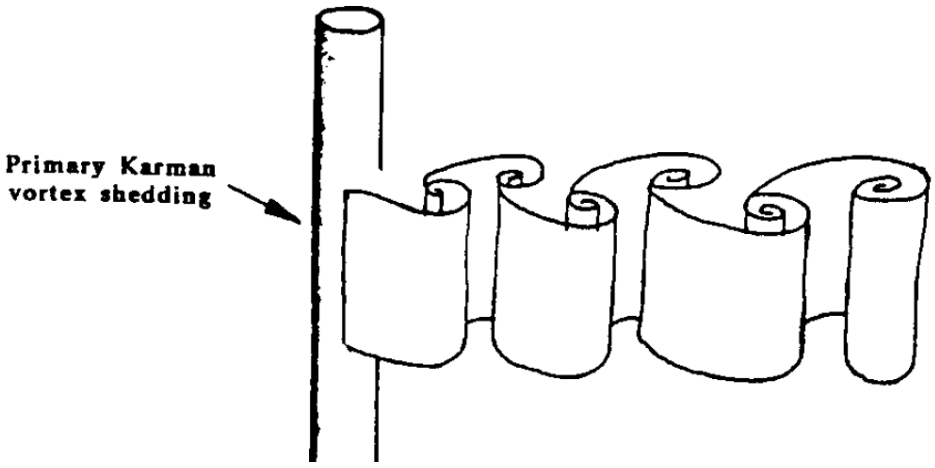

Figure 1.2: This is figure 5 from C. H. K. Williamson (1996). Illustration of two-dimensional Karman vortex shedding at $50 < Re < 140 - 194$.

This periodic vortex shedding, also referred to as Karman vortex shedding, is the cause for a fluctuating lift- and drag force on the cylinder. This is because the pressure distribution around the cylinder undergoes a periodic change as the shedding progresses, resulting in a periodic variation in the force components on the cylinder (Sumer & Fredsøe, 2006). For $Re < 50$ there is no fluctuating forces, as the recirculating vortices does not have an asymmetric periodic variation.

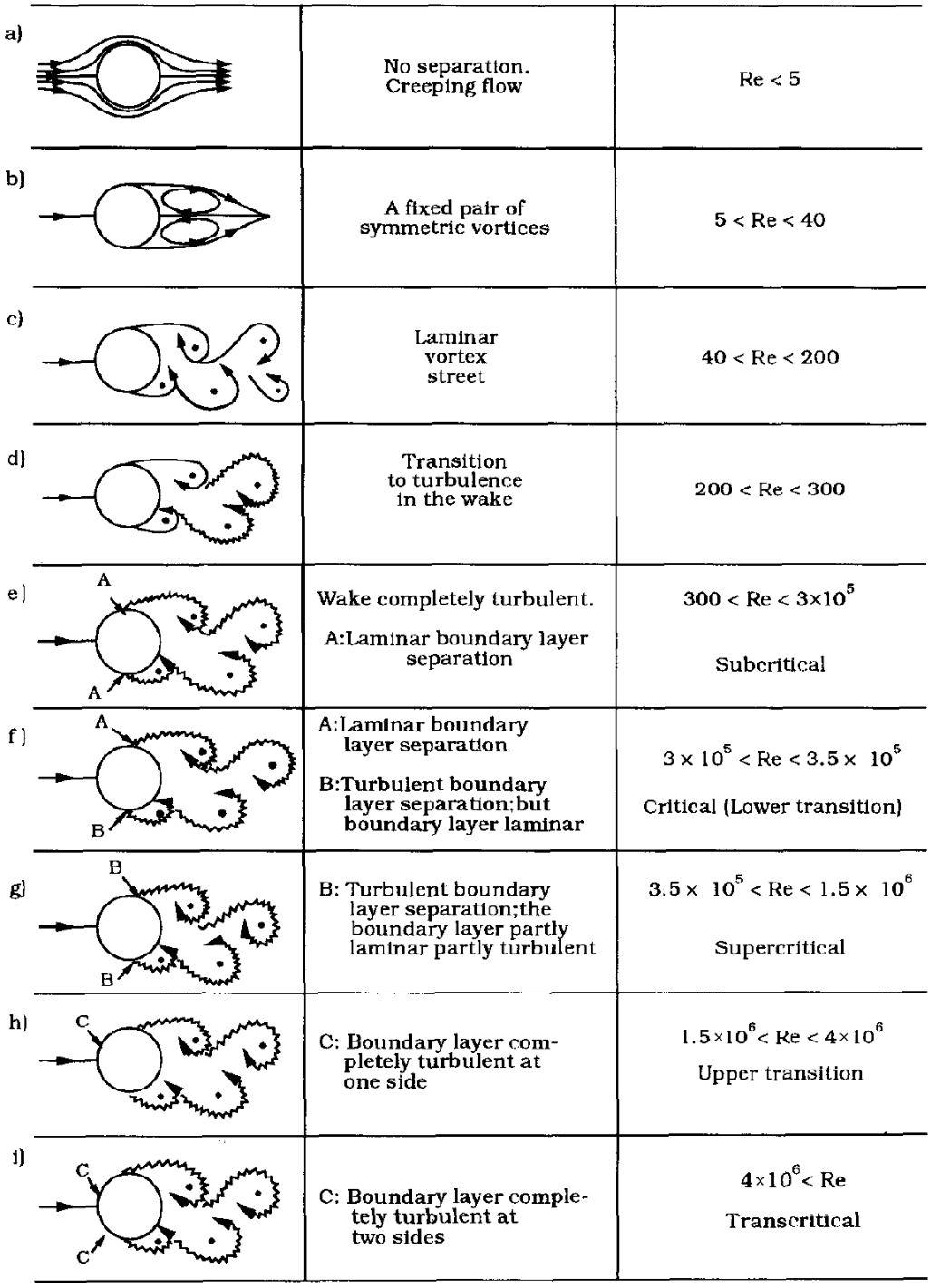

Figure 1.3: This is figure 1.1 in Sumer and Fredsøe (2006). Illustration of flow regimes around a circular cylinder in steady flow.

The vortex shedding in the wake behind a single step cylinder differs from that of a uniform cylinder. The two important parameters for the wake behind a single step cylinder are Re_D, which is the Reynolds number for the large cylinder, and D/d, which is the diameter ratio between the large- and small cylinder diameter. Based on these two parameters, the flow behind the step cylinder appears in two different modes; the direct- and the indirect mode. The direct mode occurs for $D/d < 1.25$, where the vortices that shed on the small- and large cylinder interact in a very narrow region. For $D/d > 1.55$, the indirect mode occurs, where there are now three cells that have a distinct shedding frequency (Tian et al., 2020). The S- and L-cell are the two main cells, and represent the shedding behind the small- and large cylinder respectively. The S-cell has a higher shedding frequency than the L-cell. In the wake near the step, there is a now a distinct "modulation zone" behind the large cylinder with a lower shedding frequency. This "modulation zone" is referred to as the N-cell (Dunn & Tavoularis, 2006). In the N-cell there are complex vortex interactions and a three-dimensionality to the vortex structures. The S-, N-, and L-cell in the wake behind a single step cylinder are illustrated in figure 1.4 and an experimental visualization conducted by Dunn and Tavoularis (2006) is presenting the cells in figure 1.5.

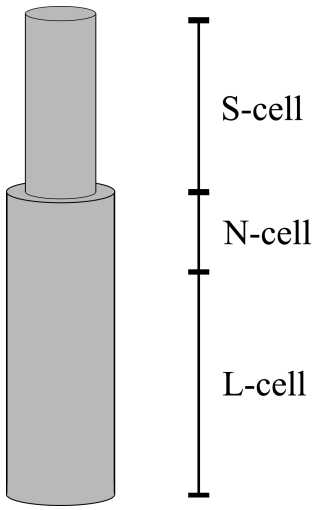

Figure 1.4: Illustration of the S-, N- and L-cell in the wake behind a single step cylinder. In the S- and L-cell the vortices are two-dimensional and shedding at two distinct frequencies. In the N-cell there are complex vortex interactions and a three-dimensionality to the vortex structures.

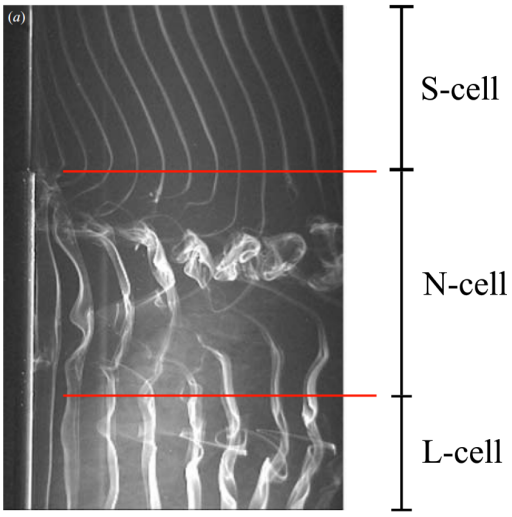

Figure 1.5: This is figure 3 (a) from Dunn and Tavoularis (2006). Experimental visualization of the S-, N- and L-cell in the wake behind a single step cylinder with $D/d = 1.96$ at $Re_D = 152$. The complexity of the N-cell is highlighted with this figure.

The properties that are important to the wake behind a dual step cylinder, illustrated in figure 1.1(b), are the diameter ratio D/d, which is the ratio between the large- and small cylinder diameter, and the aspect ratio L/D, which is the ratio between the length and the diameter of the large cylinder.

McClure et al. (2015) studied dual step cylinders in laminar low Re flow at $Re_D = 150$ with multiple different diameter- and aspect ratios. The findings showed that varying D/d and L/D lead to notable changes in the wake behind the steps and in the wake behind the large cylinder. With a decreasing D/d, the small cylinder vortices grew in strength and decreased in frequency, nearing the strength and frequency of the large cylinder vortices. With an increasing D/d, the vortices in the wake of the large cylinder became increasingly deformed. With a decreasing L/D, the vortices shed on the small cylinders connected across the wake of the large cylinder more frequently. By varying the diameter- and aspect ratios, the fluctuating forces on the cylinder also varied. Ji et al. (2020) also studied dual step cylinders at $Re_D = 200$ and examined how the vortex structures changed as D/d was varied. Ji et al. (2020) found that the force coefficients on the large cylinder were smaller than that of a uniform cylinder at the same Re, and decreased with an increasing D/d.

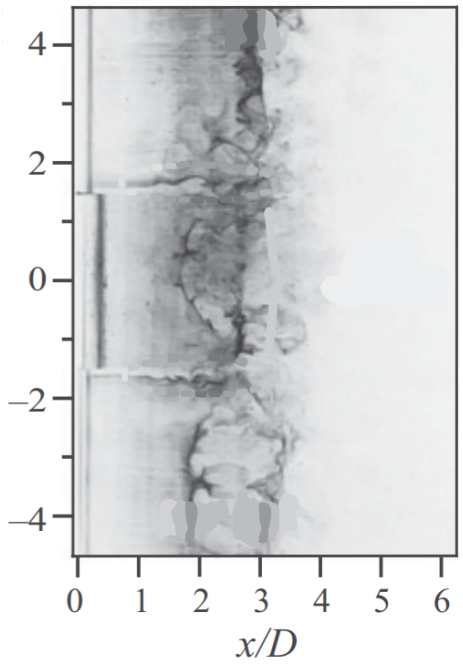

Figure 1.6: This is figure 7 (b) from Morton and Yarusevych (2020). The symbols of the figure are removed as to make the figure compatible with the present paper. Experimental visualization of the complex vortices in the flow past a dual step cylinder with $L/D = 3$ and $D/d = 2$ at $Re_D = 2.1 \times 10^3$.

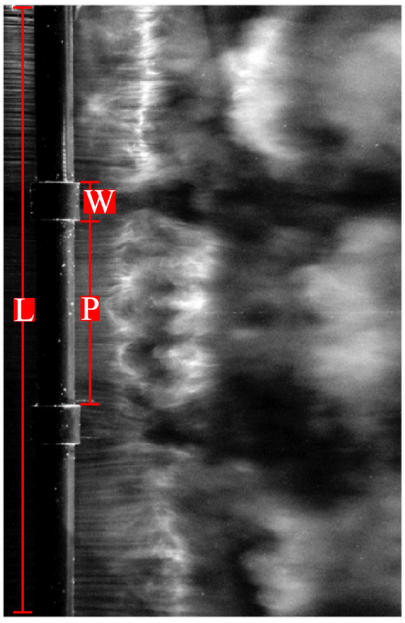

Figure 1.7: This is figure 5 (b) from Nakamura and Igarashi (2008). The symbols of the figure are added as to facilitate a detailed discussion. Experimental visualization of the flow past a multi step cylinder with $D/d = 1.3$, $W/d = 1$, $P/d = 6$, L/d at $Re_d = 2 \times 10^4$.

In figure 1.6 an experimental visualization of the vortices in the flow behind a dual step cylinder with $L/D = 3$ and $D/d = 2$ at $Re = 2.1 \times 10^3$, conducted in Morton and Yarusevych (2020), is presented. The results from McClure et al. (2015) indicated that for a dual step cylinder with $L/D = 5$

and $D/d = 1.33$ there was an $\approx 85\%$ reduction in the non-phase corrected root-mean-square (rms) value of the fluctuating lift force, and for other lower aspect ratios there was found up to 5% reduction in the mean drag force, compared to the forcing on a uniform cylinder. McClure et al. (2015) were the first to observe a reduction in the mean drag force on a dual step cylinder in laminar low Re flow. By attaching multiple large cylinder parts, the step cylinder configuration is a multi-step cylinder, illustrated in figure 1.1(c). McClure et al. (2015) suggested that the reduction in the fluctuating forces on the dual step cylinder could be maintained, or even improved, with the multi step cylinder configuration. In figure 1.7, an experimental visualization of the flow behind a multi step cylinder, conducted in Nakamura and Igarashi (2008), is presented. Similar to the dual step cylinder, Tian et al. (2022) studied the I step cylinder, which is the inversion of the large- and small cylinder diameter of a dual step cylinder geometry, illustrated in figure 1.1(d). The properties that are important to the wake behind the I step cylinder are the diameter ratio D/d, which is the same as in the dual step cylinder, and the aspect ratio l/D, which is the ratio between the length of the small cylinder in the mid span of the I step cylinder and the diameter of the large cylinders. Just like in McClure et al. (2015), the findings showed that varying l/D lead to notable changes in the wake behind the steps and in the wake behind the small cylinder.

This thesis will study dual step cylinders in uniform low Re flow at $Re = 150$. There are three different dual step cylinders with aspect ratios $L/D = 1, 3$ and 5 that are studied, all with the same constant diameter ratio $D/d = 1.33$. The full length of the dual step cylinder is constant for all three aspect ratios. The topic of this thesis will be how the wake topology and structural loading changes by varying the aspect ratio, compared to the structural loading on a uniform cylinder, and observe if there are some optimal geometrical parameters. The inspiration for this topic comes from the findings of McClure et al. (2015), discussed earlier in this chapter. In McClure et al. (2015), it was found that for a dual step cylinder with $L/D = 5$ and $D/d = 1.33$ there was an $\approx 85\%$ reduction in the non-phase corrected rms value of the fluctuating lift force, and for other lower aspect ratios there was found up to 5% reduction in the mean drag force, compared to the forcing on a uniform cylinder. This is understood from figure 14(b) in McClure et al. (2015), where the effects of keeping $L/D = 5$ constant and varying D/d was presented. Figure 14(a) in McClure et al. (2015) presented the effects of keeping $D/d = 2$ constant and varying L/D. As McClure et al. (2015) were the first to observe a reduction in the mean drag force for flow past a dual step cylinder in laminar low Re flow, and the topic of drag reduction techniques is very important, this thesis will further study how the mean drag and rms lift are affected by varying L/D with a constant $D/d = 1.33$, which was the optimal D/d based on the findings of McClure et al. (2015). This thesis will also study a dual step cylinder with $L/D = 1$ and $D/d = 2$ and compare the findings to the findings of McClure et al. (2015).

As the dual step cylinder is often used by engineers, it is important to be

able to relate it to a practical use-case in the industry. An example could be how a riser element on a pipe section affects the structural loading on the pipe section, or how the base of a floating oil rig could be designed as a dual step cylinder to decrease the structural loading due to currents and waves. In both these examples, one would expect the engineers to have a certain length of a pipe section or the length of the base of the floating oil rig planned. That is why, to better relate to a practical use-case, this thesis will study the effects of changing the aspect ratio of a dual step cylinder with a fixed length.

By understanding how changing the aspect ratio of the dual step cylinder affects the structural loading in this thesis, the results can be compared to other previous design choices that passively reduce the forcing compared to a uniform cylinder. Bearman and Owen (1998) studied the flow behind a two-dimensional rectangular cylinder having sinusoidal front and rear faces, and it is illustrated in figure 1.8. Compared to the equivalent two-dimensional straight cylinder model, drag reductions up to 30% were achieved at $Re \approx 4 \times 10^4$. Bearman and Owen (1998) also stated that for $0.06 \leq w/L \leq 0.09$, where w is two times the amplitude of the sinusoidal faces, vortex shedding was completely suppressed, but say nothing of the lift force. Not too different were Lee and Nguyen (2007), where instead of a two-dimensional rectangular cylinder having sinusoidal front and rear faces, a sinusoidal cylinder was studied, as illustrated in figure 1.9. For certain design parameters in the design, a 22% reduction in drag, compared to a uniform cylinder, was achieved at $Re = 10^4$. The reduction in lift was also not mentioned, but Lee and Nguyen (2007) stated that the vortex induced fluctuations were suppressed.

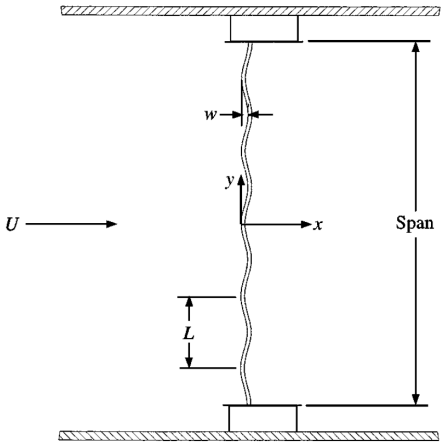

Figure 1.8: This is figure 1 from Bearman and Owen (1998). Diagram of the two-dimensional rectangular cylinder having sinusoidal front and rear faces.

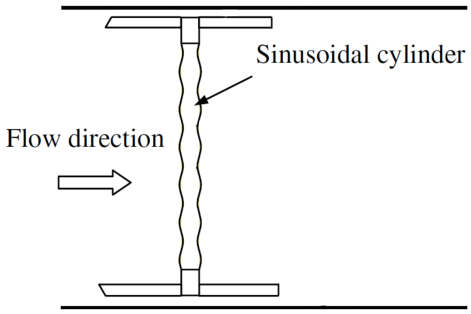

Figure 1.9: This is figure 2 from Lee and Nguyen (2007). Diagram of the sinusoidal cylinder.

Owen et al. (2001) studied the flow past a cylinder with a constant circular cross-section and a sinusoidal axis, as well as the flow past a cylinder with

hemispherical bumps, as illustrated in figure 1.10. For the circular cylinder with a sinusoidal axis, a drag reduction of 47% was achieved at $Re = 3.3 \times 10^4$. The cylinder with hemispherical bumps achieved a steady 25% drag reduction at $10^4 \leq Re \leq 10^5$. For both cases it was reported that there were suppression of vortex shedding. Yoon et al. (2019) studied the flow past a twisted cylinder, illustrated in figure 1.11, and the results are showing that the drag reduction steadily increased as Re increased. At $Re = 3 \times 10^3$, the drag reduction was 13% and at $Re = 10^4$, the drag reduction was 28%. The rms lift was greatly reduced and relatively independent of Re. At $Re = 3 \times 10^3$ and $Re = 10^4$ the rms lift reduction was 95% and 97% respectively.

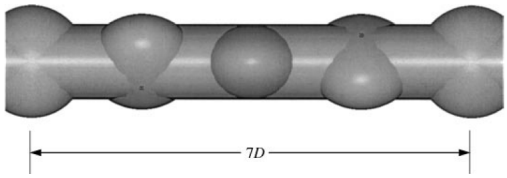

Figure 1.10: This is figure 3 from Owen et al. (2001). Geometry of the cylinder with hemispherical bumps.

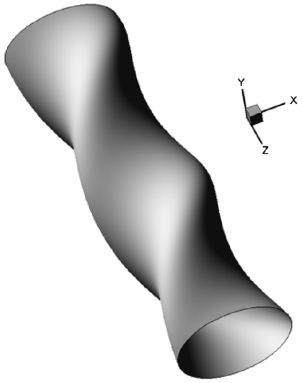

Figure 1.11: This is figure 1(a) from Yoon et al. (2019). Geometry of the twisted cylinder.

Nakamura and Igarashi (2008) studied a circular cylinder with cylindrical rings along its span, or a multi-step cylinder as it is called in this thesis. Illustration of the circular cylinder with cylindrical rings along its span is found in figure 1.12. For the optimal parameters of the study, a drag reduction of 15% was achieved at $Re_d \approx 3 \times 10^5$. Under approximately the same values for Re, the fluctuating lift energy was reduced by one third.

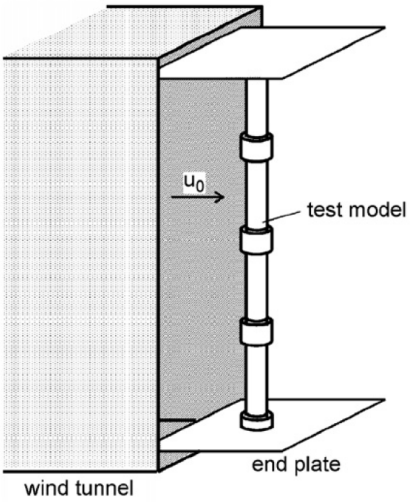

Figure 1.12: This is figure 1(a) from Nakamura and Igarashi (2008). Diagram of circular cylinder with cylindrical rings along its span.

The differences between this thesis and the previous studies mentioned is that the optimal results for the different geometrical configurations that have been investigated were investigated at $\approx 3 \times 10^3 \leq Re \leq 10^5$, which was a turbulent high Re flow. This thesis will investigate a laminar low Re flow at $Re_D = 150$. Although not all studies mention the reduction

in rms lift, Yoon et al. (2019) achieved 97% at $Re = 300$ which was the highest. Even if there were good reductions in both the drag and rms lift, some of the geometries would be difficult to make in practice, whereas a dual step cylinder is simple to weld in comparison.

This thesis is organized in four chapters. Chapter 1 is the introduction. In chapter 2, the flow problem and the numerical settings are addressed in addition to the convergence tests. Chapter 3 is divided into three parts. The first part discusses the differences in the wake flow and the structural loading on a dual step cylinder with $L/D = 1$ and $D/d = 2$ at $Re_D = 150$ between this thesis and McClure et al. (2015). The second and third part analyses the features of the wake flow and structural loading of three dual step cylinders with $L/D = 1, 3$ and 5 and $D/d = 1.33$, and discusses the effects of varying L/D on a dual step cylinder. In chapter 4, the summary and conclusion of this thesis is presented, as well as the interesting points that can be further studied in future work.

CHAPTER 2

Governing equations, computational method and convergence study

2.1 Computational method

The incoming flow is uniform in the positive x-direction, and the Reynolds number based on the large cylinder diameter is $Re_D = 150$ for all simulations. The origin of the coordinate system is in the middle of the large cylinder, as shown in figures 2.1.1 and 2.1.2. The incompressible flow is governed by the continuity equation and the time-dependent three-dimensional incompressible Navier-Stokes equation

$$\boldsymbol{\nabla} \cdot \mathbf{u} = 0, \tag{2.1}$$

$$\frac{\partial \mathbf{u}}{\partial t} + (\mathbf{u} \cdot \boldsymbol{\nabla})\mathbf{u} = \nu \nabla^2 \mathbf{u} - \frac{1}{\rho}\boldsymbol{\nabla} p, \tag{2.2}$$

where ρ is the constant fluid density, $\mathbf{u}$ is the velocity vector, p is the pressure and t is time (Tian et al., 2023b).

All the direct numerical simulations in this thesis were conducted by the thoroughly validated finite-volume numerical code MGLET (Manhart, 2004). A staggered Cartesian grid is used, where the velocities are calculated on the middle of the grid faces, whilst the pressure is calculated in the middle of the grid cell. The midpoint rule is used to approximate the surface integral, leading to second-order accuracy. The solid surface of the step cylinder is handled by an immersed boundary method (Peller et al., 2006). Recent examples of this code being applied for studies of other complex flows includes the flow over a single dimple recessed in a flat plate (Zhu et al., 2024), the coexistence of natural and forced vortex dislocations in step cylinder flow (Tian et al., 2023a) and the wake behind a concave curved cylinder (Jiang et al., 2018). For the time integration, a third-order explicit Runge-Kutta scheme

(J. H. Williamson, 1980) is applied with a constant time step Δt that ensures a CFL (Courant-Friedrichs-Lewy) number smaller than 0.5. By solving a Poisson equation with Stone's implicit procedure (Stone, 1968), the elliptic pressure–velocity coupling is handled. The computational domain is initially evenly divided into cubic grid boxes, referred to as level-1 boxes, with N × N × N equally sized cubic grid cells in each. To enhance precision for capturing complex flow phenomena near structures like the dual step cylinder surface and areas where vortices form, such as near the steps, the grid is refined by continually splitting the level-1 box. The grid cell of each face is doubled such that each level-1 box contains eight N × N × N equally sized cubic grid cells termed level-2 boxes. This refinement process continues until reaching the maximum specified grid level, which is six in all simulations conducted in this thesis. The xz- and xy-plane of the grid used for case Fine-B in table 2.1.1 is presented in figure 2.1.1 and 2.1.2 respectively, where the level 1-6 grid boxes are illustrated and shows how the transition from layer to layer is conducted.

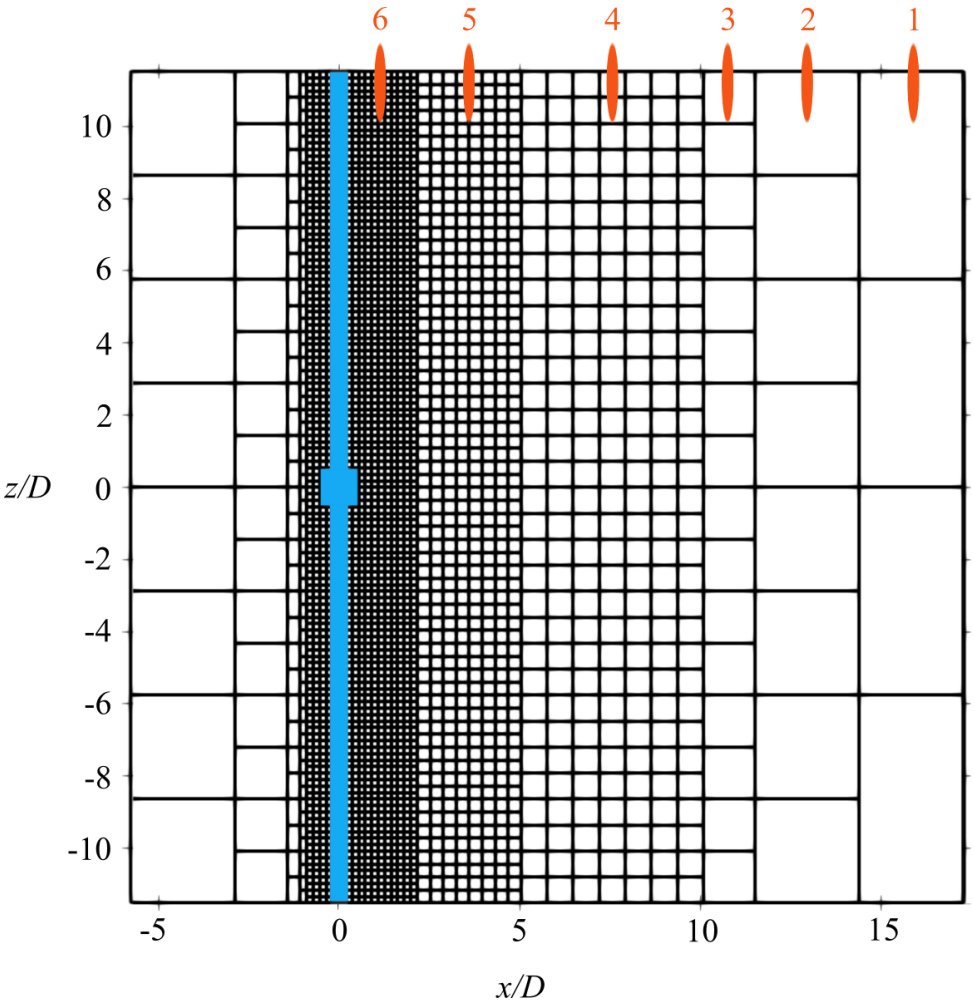

Figure 2.1.1: Illustration of the multi-level grids in the xz-plane at $y/D = 0$. Each square represents a slice of the corresponding cubic Cartesian grid box that contains $N \times N \times N$ grid cells. The six levels of grid boxes are highlighted in orange. This illustration is from case Fine-B.

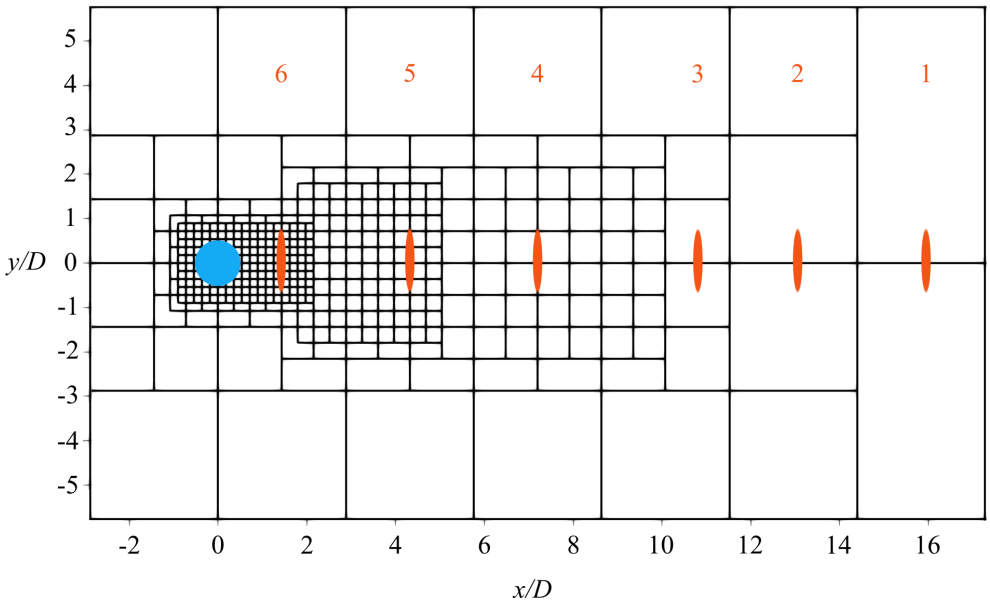

Figure 2.1.2: Illustration of the multi-level grids in the xy-plane at $z/D = 0$. Each square represents a slice of the corresponding cubic Cartesian grid box that contains $N \times N \times N$ grid cells. The six levels of grid boxes are highlighted in orange. This illustration is from case Fine-B.

l/D	Case	Min. cell size Δ_c/D	Domain size $(L_x \times L_y \times L_z)/D$	L/D	D/d	Grids ($\times 10^8$)
11.02	Coarse	0.015	$51.84 \times 34.56 \times 23.04$	1	2	0.60
10.70	Medium	0.0125	$50.40 \times 33.60 \times 22.40$	1	2	0.97
11.02	Fine-B	0.01	$51.84 \times 34.56 \times 23.04$	1	2	2.01
16.78	Fine-C	0.01	$51.84 \times 34.56 \times 34.56$	1	2	3.01
5.26	Fine-A	0.01	$51.84 \times 34.56 \times 11.52$	1	2	1.01

Table 2.1.1: Mesh and computational domain information of all simulations in the convergence tests. The cases Fine-A, Fine-B and Fine-C are used for the spanwise length study to determine domain convergence. The cases Coarse, Medium and Fine-B are used for the grid study. The Reynolds number for all simulations is $Re_D = 150$.

Both the grid convergence- and domain convergence study are conducted based on a dual step cylinder with $L/D = 1$ and $D/d = 2$, and table 2.1.1 gives an overview of the numerical simulations that are conducted in those studies. Each row in the table in order presents the non-dimensional length of the small cylinders l/D above and below the large cylinder, the case name, the smallest cell size in the grid Δ_c/D, the size of the computational domain $(L_x \times L_y \times L_z)/D$ where the dual step cylinder geometry is centered at $(x = y = z = 0)$, and the number of grid cells in the simulation. The computational domain size L_x and L_y are both larger compared with Tian

et al. (2023b) and Tian et al. (2020) for a single-step cylinder with the same Re_D, therefore only a spanwise convergence study has been conducted. The three cases denoted Coarse, Medium and Fine-B are selected for the grid convergence study, and for the spanwise convergence study the Fine-A, Fine-B and Fine-C cases are used.

In this thesis, the calculation of the force coefficients over the whole span of the dual step cylinder is done in two different ways. It is important to differentiate the two methods as they can be misleading if not properly defined and understood. The first method is to calculate the force coefficients based upon the certain body that is investigated, and the second method is to calculate the force coefficients based upon a body that is being compared against. The first method is defined in equation 2.3 and 2.4,

$$C_D^*(t) = \frac{2F_D(t)}{A_{dual}} \tag{2.3}$$

$$C_L^*(t) = \frac{2F_L(t)}{A_{dual}} \tag{2.4}$$

where the force coefficient time series $C_D^*(t)$ and $C_L^*(t)$ are defined based on the area of the whole dual step cylinder, as $A_{dual} = 2ld + LD$. The uniform cylinder is not considered in this calculation, and the force coefficients are purely calculated for the insight into the performance of the dual step cylinder geometry. These force coefficients will only be calculated for the simulations in table 2.1.1 to highlight how the results can be misleading when comparing the dual step cylinder to a uniform cylinder. In chapter 3.3, the second method of calculating the force coefficient time series $C_D(t)$ and $C_L(t)$ (without the asterix *) are presented in equations 3.1 through 3.6. This method disregards the extended area of the dual step cylinder, as $A = 2ld + Ld$, and allows for a direct comparison between the dual step cylinder and the uniform cylinder that will highlight if there is increased or decreased forcing when attaching the large cylinder part to a uniform cylinder.

2.2 Grid convergence

Figure 2.2.1 shows the distribution of the time-averaged streamwise velocity $\overline{u/U}$ on the sample line AB, $0.03D$ upstream from the large cylinder surface. The line AB is from $-0.49 \leq z/D \leq 0.49$. Figure 2.2.2 and 2.2.3 shows the mean drag coefficient $\overline{C_D^*}$ and the rms lift coefficient C_{LRMS}^*, respectively, for the small cylinder at $z/D \leq -0.5$ in the left plot, the large cylinder in the middle plot and the small cylinder at $z/D \geq 0.5$ in the right plot. The middle plot has a different scale on the vertical axis. The largest difference between the Medium case and the Fine-B case is 5.0% near $z/D = \pm 2$, compared to the much larger difference between the Coarse and Medium case. Figure 2.2.1, 2.2.2 and 2.2.3 clearly show a convergent tendency from the Coarse case to the Fine-B case. According to these considerations, the grid refinement of case Fine-B is sufficiently fine to accurately simulate the flow around the dual step cylinders in this thesis.

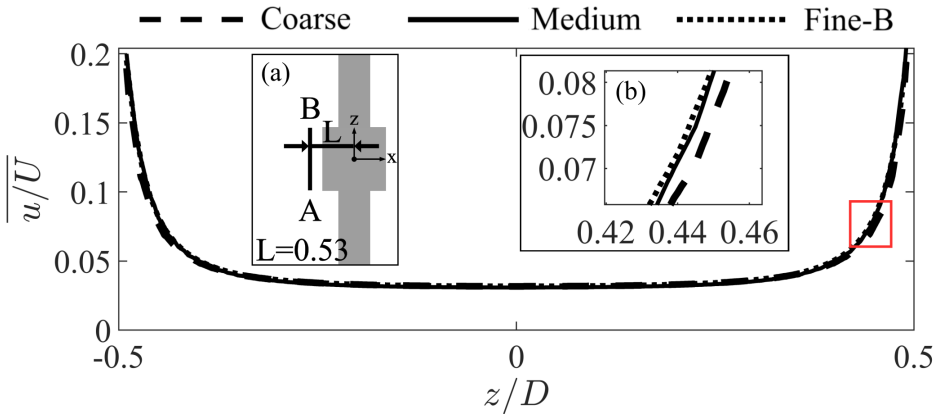

Figure 2.2.1: Distributions of time-averaged streamwise velocity $\overline{u/U}$, sampled on line AB, $0.03D$ downstream the large cylinder. Inset (a) shows a sketch of the position of the sampling line AB of length $0.98D$ from $-0.49 \leq z/D \leq 0.49$. Inset (b) is a zoomed in view of the red rectangle. The different cases are denoted Coarse, Medium and Fine-B.

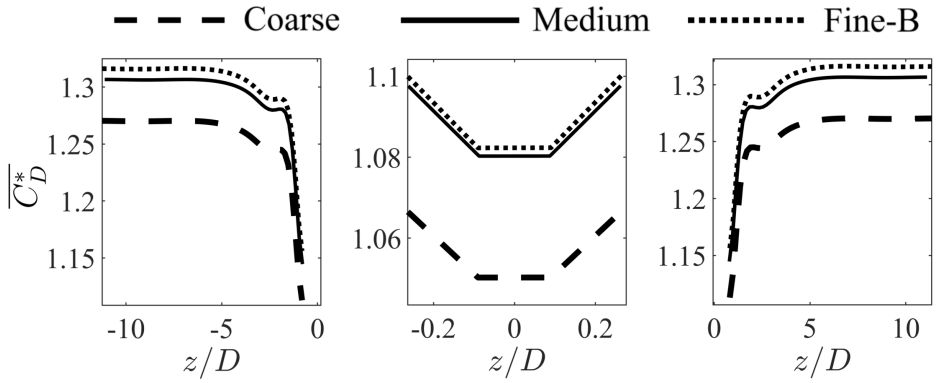

Figure 2.2.2: Distribution of the mean drag coefficient $\overline{C_D^*}$ for the small cylinder at $z/D \leq -0.5$ in the left plot, the large cylinder in the middle plot and the small cylinder at $z/D \geq 0.5$ in the right plot. The cases Coarse, Medium and Fine-B represent different grid refinements.

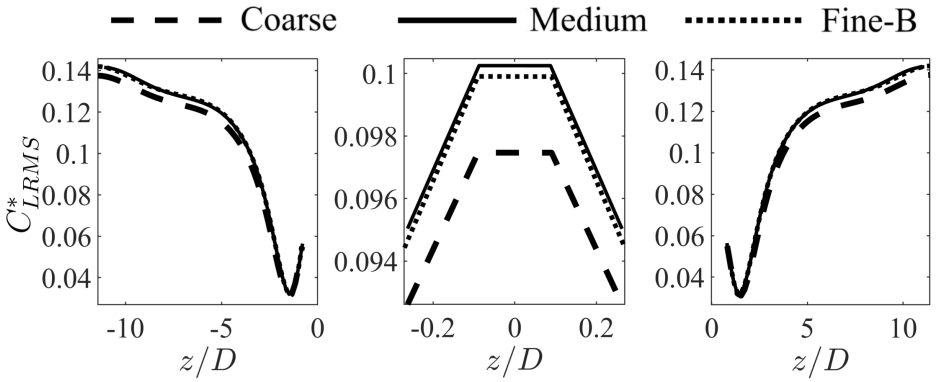

Figure 2.2.3: Distribution of the rms lift coefficient C_{LRMS}^* for the small cylinder at $z/D \leq -0.5$ in the left plot, the large cylinder in the middle plot and the small cylinder at $z/D \geq 0.5$ in the right plot. The cases Coarse, Medium and Fine-B represent different grid refinements.

2.3 Spanwise length convergence

The spanwise length convergence was studied, using the same grid structures as in case Fine-B, by changing the length of the small cylinder l/D above and below the large cylinder. See table 2.1.1 for the two other simulations, Fine-A and Fine-C, applied in the spanwise length convergence study. Figure 2.3.1 and 2.3.2 shows the spanwise distribution of $\overline{C_D^*}$ and C_{LRMS}^*, respectively, in the region $-12 \leq z/D \leq 12$. For the small cylinder at $z/D \leq -0.5$ in the left plot, the large cylinder in the middle plot and the small cylinder at $z/D \geq 0.5$ in the right plot. The middle plot has a different scale on the vertical axis. In figure 2.3.2, the results indicate that the free-slip wall boundary condition affects the result for C_{LRMS}^* strongly for the Fine-B results at $z/D \approx -8/8$, but the largest difference to Fine-C before those points is 1.72% at $z/D = 0.27$. Based on the convergent tendency of figure 2.3.2, we can convincingly say that the spanwise length in the Fine-A converge well in the whole region and Fine-B cases converge well in the domain $z/D = -8/8$.

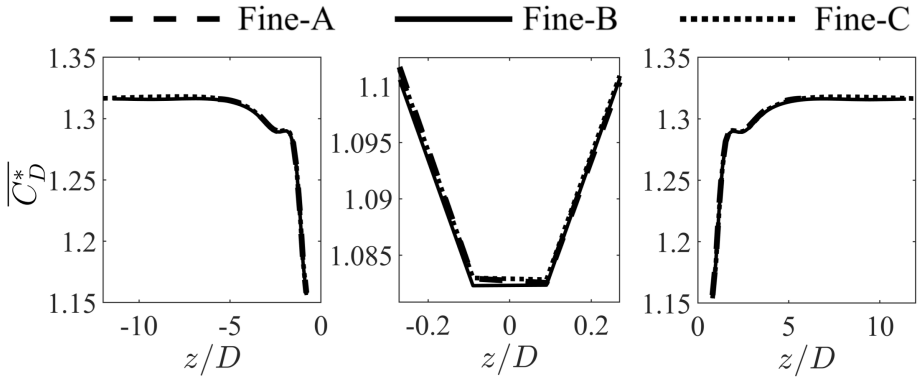

Figure 2.3.1: Distribution of the time-averaged mean drag coefficient $\overline{C_D^*}$ for the small cylinder at $z/D \leq -0.5$ in the left plot, large cylinder in the middle plot and the small cylinder at $z/D \geq 0.5$ in the right plot. The cases Fine-C, Fine-B and Fine-A represent different l/D ratios.

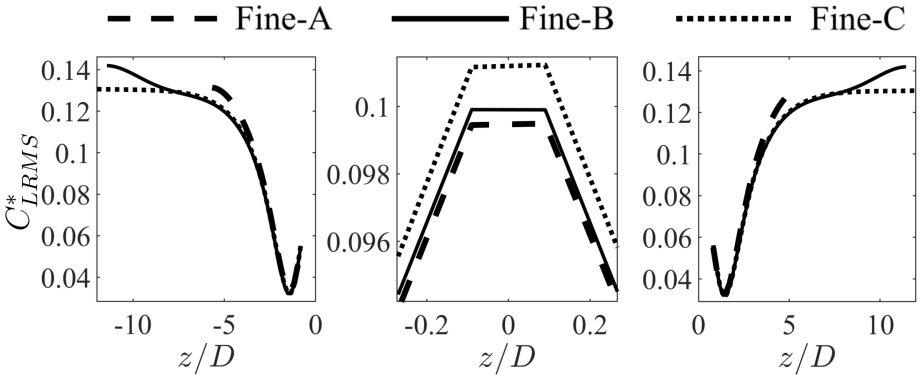

Figure 2.3.2: Distribution of the rms lift coefficient C_{LRMS}^* for the small cylinder at $z/D \leq -0.5$ in the left plot, large cylinder in the middle plot and the small cylinder at $z/D \geq 0.5$ in the right plot. The cases Fine-C, Fine-B and Fine-A represent different l/D ratios.

2.4 Simulation overview

In table 2.4.1, the dual step cylinder geometry, mesh information and the computational domain of all simulations that have been conducted for the aspect ratio study in chapter 3.2 and 3.3 are presented.

Case	L/D	l/D	D/d	Domain size $(L_x \times L_y \times L_z)/D$	Min. cell size Δ_c/D	Grids $(\times 10^8)$
L1	1	16.78	1.33	$51.84 \times 34.56 \times 34.56$	0.01	3.01
L3	3	15.78	1.33	$51.84 \times 34.56 \times 34.56$	0.01	3.01
L5	5	14.78	1.33	$51.84 \times 34.56 \times 34.56$	0.01	3.01

Table 2.4.1: Dual step cylinder geometry, mesh and computational domain information of all simulations in the aspect ratio study in chapter 3.2 and 3.3. The cases L1, L3 and L5 are denoted based on the aspect ratio L/D. The Reynolds number for all simulations is $Re_D = 150$.

In figure 2.4.1$(a) - (c)$, cases L1, L3 and L5 are illustrated respectively. All three cases L1, L3 and L5 in table 2.4.1 represents the same pipe of length $z/D = 25.2$, but with different aspect ratios on the large cylinder.

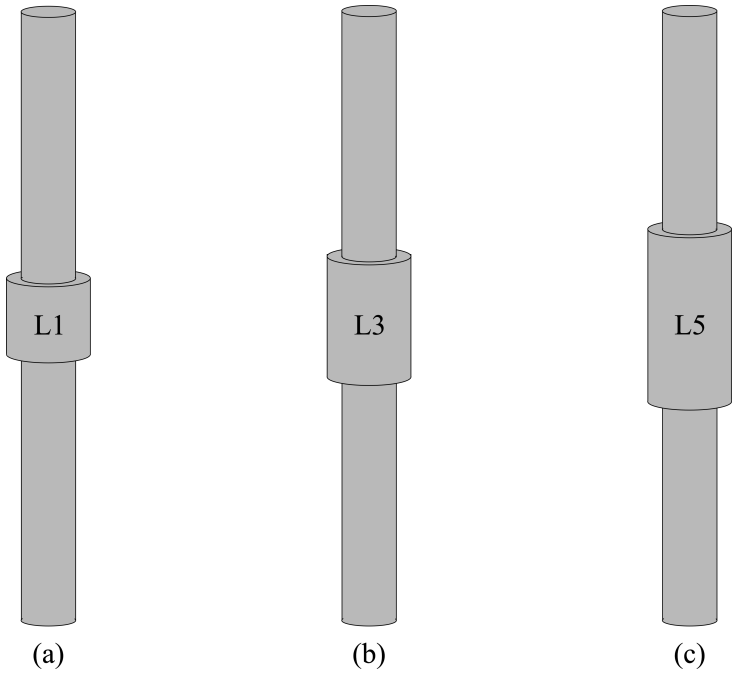

Figure 2.4.1: Illustration of the geometrical configuration of cases L1, L3 and L5.

Based on the spanwise length study in figure 2.3.2, the domain size from simulation Fine-C is chosen to be applied in all simulations in table 2.4.1. Simulation Fine-B and Fine-C both converged together up until $\approx z/D = \pm 8$ where the boundary effects affected simulation Fine-B. Therefore, to be able

to simulate a longer cylinder than Fine-B would allow us to, due to the boundary effects, the domain size of Fine-C is selected. The pipe length of $z/D = 25.2$ is selected to avoid the boundary effects in simulation Fine-C. Since simulation Fine-C has a larger D/d than the simulations in table 2.4.1 and the grid converged, we can say that the grid is fine enough to be applied to the simulations in table 2.4.1. This is because the vortex structures are less chaotic with a smaller D/d.

CHAPTER 3

Results and discussion

This chapter has three parts. In chapter 3.1, the results from McClure et al. (2015) are compared to the results of this thesis for a dual step cylinder with $D/d = 2$ and $L/D = 1$ at $Re_D = 150$, and the differences are discussed. In chapter 3.2 and 3.3, three dual step cylinders with $D/d = 1.33$ and $L/D = 1, 3$ and 5 at $Re_D = 150$ are studied. In chapter 3.2, how the features of the wake flow are affected by varying L/D is discussed, and in chapter 3.3, what the effects of varying L/D are on the structural loading is discussed and the results are compared to that of a uniform cylinder.

3.1 Comparisons with the results by McClure et al. (2015)

McClure et al. (2015) presents for the dual step cylinder with aspect ratio $L/D = 1$ and diameter ratio $D/d = 2$ that $C_{LRMS} = 0.012$ and $\overline{C_D} = 1.06$ on the large cylinder part. This was presented in figure $9(c)$ and $9(d)$ in McClure et al. (2015). Case Fine-B from the spanwise convergence study, which is found in table 2.1.1 in chapter 2.1, has the same geometrical properties as the aforementioned dual step cylinder. In case Fine-B, the force coefficients on the large cylinder are $C_{LRMS} = 0.097$ and $\overline{C_D} = 1.06$. Force coefficients on the large cylinder are based on the large cylinder diameter D. For case Fine-B, the value for C_{LRMS} on the large cylinder is eight times larger than in McClure et al. (2015). The question becomes; what is the reason for this substantial difference? In figure 3.1.1 the vortex structures from McClure et al. (2015) for the dual step cylinder with $L/D = 1$ and $D/d = 2$ are presented. From that, McClure et al. (2015) stated that any distinct shedding of spanwise vortices from the large cylinder ceases, and the large cylinder essentially acts to induce vortex dislocations by reducing the convective velocity of the small cylinder vortices. This can be seen at $(x/D, z/D) = (4, 0)$ in the far wake behind the large cylinder and beyond in figure 3.1.1, where the small cylinder vortices are bent inward and do not cross the wake behind

the large cylinder, as the convective velocity is reduced in that section of the wake. In figure 3.1.2, the vortex structures from case Fine-B are presented. In contrast to figure 3.1.1, there are complex vortex loops and vortex interactions in both the near and far wake behind the large cylinder. In figure 3.1.2, one vortex loop that is seen from case Fine-B, but not in figure 3.1.1 by McClure et al. (2015), is at $(-0.5 \leq z/D \leq 0.5, 4 \leq x/D \leq 7)$.

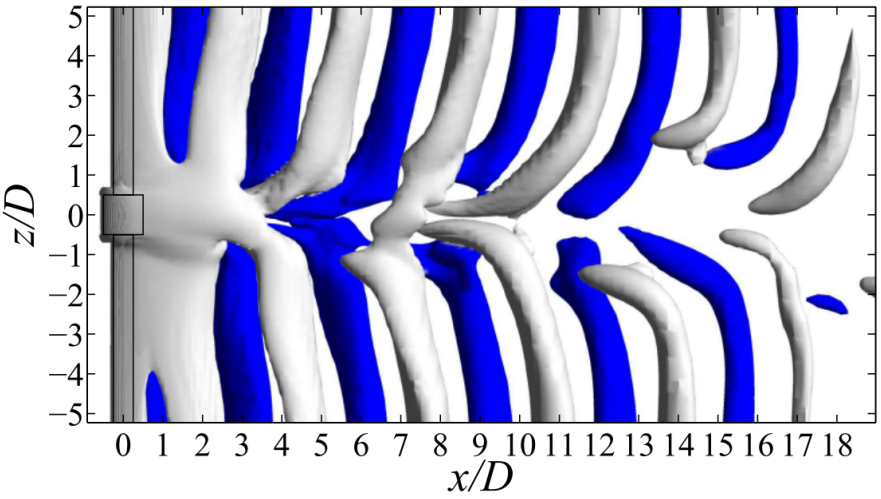

Figure 3.1.1: This is figure 6(c) in McClure et al. (2015). Instantaneous isosurfaces of $\lambda_2 = 0.01$ from McClure et al. (2015) for dual step cylinder with $L/D = 1$ and $D/d = 2$, which are the same dimensions as in case Fine-B. The color of the vortex surface represents the sign of the z-component of the vorticity.

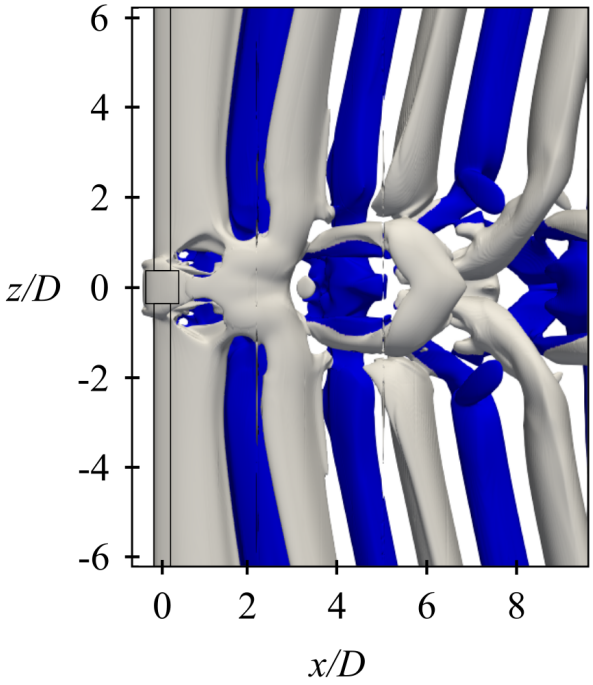

Figure 3.1.2: Instantaneous isosurfaces of $\lambda_2 = -0.01$ for case Fine-B at $tU/D = 600$. The color of the vortex surface represents the sign of the z-component of the vorticity.

In figure 3.1.3, the spanwise contour plot of the vorticity in the xy-plane at spanwise position $z/D = 0$ from McClure et al. (2015) is presented for the dual step cylinder with $L/D = 1$ and $D/d = 2$. Based on the results from figure 3.1.3, the vorticity seems to be very symmetrical due to the vorticity of different sign barely crossing the $y/D = 0$ line. The first instance where the vorticity of different sign cross the $y/D = 0$ line is at $(x/D, y/D) = (6, 0)$ in figure 3.1.3. At this point in the far wake behind the large cylinder, the vorticity has greatly dissipated and is not as strong as it was in the near wake, such as at $(x/D, y/D) = (2, -0.75)$ in figure 3.1.3. In figure 3.1.4, the spanwise contour plot of the vorticity in the xy-plane at spanwise position $z/D = 0$ for case Fine-B is presented. In contrast to figure 3.1.3, the vorticity is asymmetrical due to the vorticity of different sign crossing the $y/D = 0$ line. This happens in both the near wake at $(x/D, y/D) = (2.5, 0)$, but also in the far wake at $(x/D, y/D) = (7, 0.75)$. The strength of the vorticity in the far wake is still strong in figure 3.1.4.

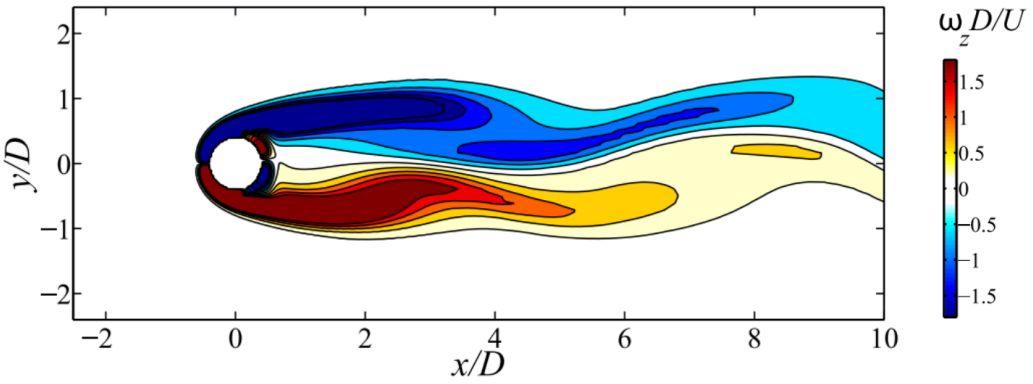

Figure 3.1.3: This is figure 11(h) in McClure et al. (2015). Spanwise vorticity contours in the xy-plane at $z/D = 0$ in the wake behind the large cylinder for a dual step cylinder with $L/D = 1$ and $D/d = 2$. Captured at unknown tU/D.

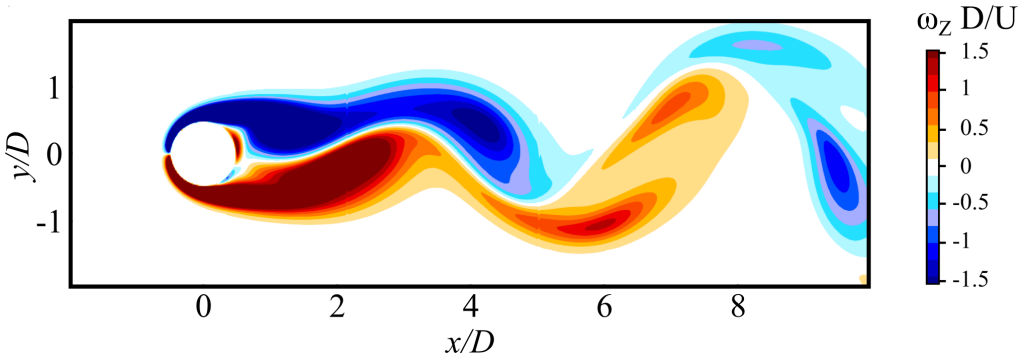

Figure 3.1.4: Spanwise vorticity contours in the xy-plane at $z/D = 0$ in the wake behind the the large cylinder for case Fine-B. Captured at $tU/D = 600$.

Both the differences in vortex structures between McClure et al. (2015) and case Fine-B observed from figure 3.1.1 and 3.1.2, and the differences in symmetry and strength in the contour plot of the vorticity between McClure et

al. (2015) and case Fine-B observed from figure 3.1.3 and 3.1.4 could explain the substantial difference in C_{LRMS} on the large cylinder. With less defined shedding, and symmetry in the vorticity in the wake of the large cylinder combined with a large dissipation in the vorticity in the far wake, the amplitude of the lift force on the large cylinder will be greatly affected as it is those factors that generate the lift force on the large cylinder. The complex vortex loops and vortex interactions in both the near and far wake behind large cylinder, and the vorticity that is asymmetric as well as strong in the far wake, that is present in case Fine-B, affects the amplitude of the lift force on the large cylinder. Those factors can explain why the C_{LRMS} value on the large cylinder is eight times larger for case Fine-B compared to McClure et al. (2015). One explanation is that the grid applied by McClure et al. (2015) could be too coarse, such that it does not capture the complexity in the flow that affects the lift force on the large cylinder; it is not clear to the authors whether a grid refinement of the step cylinders was conducted. The basis for this claim can be observed at $(x/D, y/D) = (6, 0.5)$ in figure 3.1.3 where the contour is staggered, something which is unnatural, in contrast to the smooth contour of figure 3.1.4.

Another difference, leading from the differences in the vortex structures and the vorticity in the wake behind the large cylinder, is the length and shape of the recirculation length. The recirculation length is where the streamwise velocity is zero ($U = 0$). In figure 3.1.5, the recirculation length is presented as it was in McClure et al. (2015) and can be seen as the black line. It states that the recirculation line extends to its maxima of $x/D \approx 3.5$ in the middle of the wake behind the large cylinder, and converges at $x/D \approx 1.2$ on the small cylinders. In figure 3.1.6, the recirculation length from case Fine-C, Fine-B and Fine-A from the spanwise length convergence study is presented. This shows a recirculation line that extends to a maxima of just $x/D = 2.25$ for case Fine-B, and the maxima are near the steps rather than near the center of the large cylinder wake as in McClure et al. (2015). The recirculation line converges at $x/D \approx 1.14$ on the small cylinders which is similar to McClure et al. (2015) considering that the substantial differences in results are in the wake behind the large cylinder.

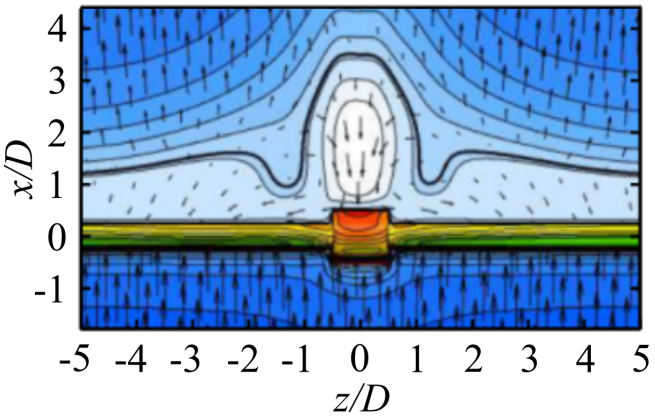

Figure 3.1.5: This is figure 11(c) in McClure et al. (2015). The recirculation length from McClure et al. (2015) of the dual step cylinder with $L/D = 1$ and $D/d = 2$. The black line represents the recirculation line.

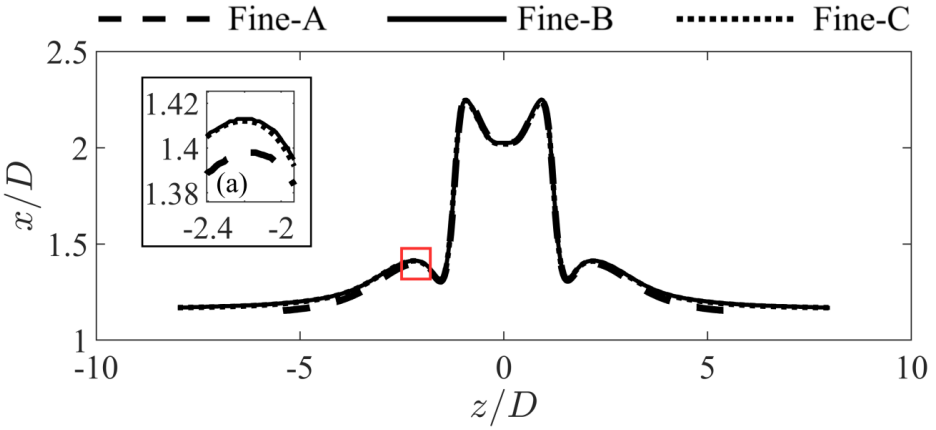

Figure 3.1.6: The recirculation length for the three cases Fine-C, Fine-B and Fine-A which represent three different l/D values. Inset (a) is a zoomed in view of the red rectangle.

McClure et al. (2015) based the results for the dual step cylinder with $L/D = 1$ and $D/d = 2$ on a simulation with a spanwise length of $-5 \leq z/D \leq 5$. In figure 3.1.6(a), our findings show that case Fine-A has not converged, since the recirculation line is different to that of case Fine-B and Fine-C, which converge nicely. Case Fine-A is of a similar domain size as the one applied by McClure et al. (2015), and case Fine-A does not converge at $z/D = -5/5$. In figure 2.3.2 from section 2.3, the free-slip boundary condition greatly affects the results for C^*_{LRMS} near $z/D = -5/5$ as well. This leads us to believe that the spanwise length applied by McClure et al. (2015) for the dual cylinder with $L/D = 1$ and $D/d = 2$ has not converged. Another reason for the difference in C_{LRMS} on the large cylinder could be that McClure et al. (2015) based the calculations on a flow that is not fully-developed. In figure 3.1.7, the lift coefficient time series $C_L(t)$ for a uniform cylinder at $Re = 75$ is presented. This is from the simulation that is used to compare the force coefficients to that of a uniform cylinder in table 3.1.1, as $Re_d = 75$. C_L is presented from $0 \leq tU/D \leq 200$ and it clearly shows how the value for C_L is

affected by the developing flow. If McClure et al. (2015) has based his results partially on a flow that is not fully-developed, it could affect the value for C_{LRMS} on the large cylinder.

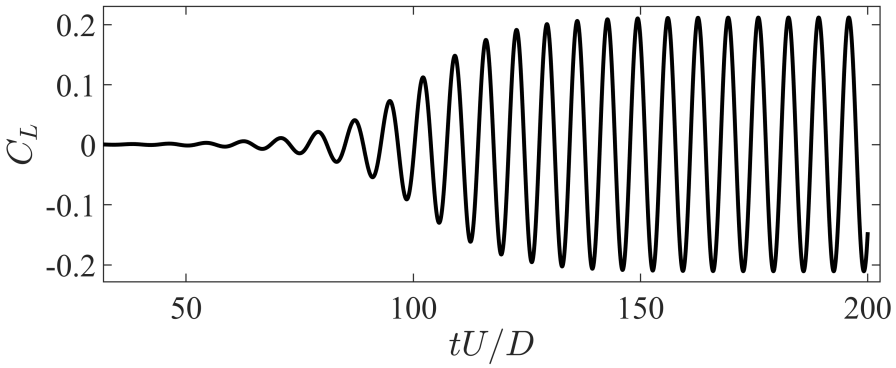

Figure 3.1.7: Lift coefficient time series $C_L(t)$ of a uniform cylinder at $Re = 75$. C_L is presented from $0 \leq tU/D \leq 200$ and presents how C_L can be affected by the developing flow.

In table 3.1.1, multiple differences between simulation Fine-B and McClure et al. (2015) for the dual step cylinder with $L/D = 1$ and $D/d = 2$ are summarized. Each row in order presents the large cylinder $\overline{C_D}$ and C_{LRMS}, and the reduction in $\overline{C_D^*}$, $\overline{C_D}$ and C_{LRMS} compared to the force coefficients of a uniform cylinder with diameter d over the whole dual step cylinder. The equation for calculating $\overline{C_D^*}$ is equation 2.3 from chapter 2.1. The equations for calculating $\overline{C_D}$ and C_{LRMS} are equation 3.3 and 3.4 from chapter 3.3. The values for the reduction from McClure et al. (2015) are read from figure 14(a) in McClure et al. (2015) and can be slightly inaccurate. The uniform cylinder simulation at $Re = 75$ gives $\overline{C_D} = 1.345$ and $C_{LRMS} = 0.149$, which are used to calculate the reduction in the force coefficient compared to that of a uniform cylinder.

Case	Large cyl. $\overline{C_D}$	Large cyl. C_{LRMS}	Reduction $\overline{C_D^*}$	Reduction $\overline{C_D}$	Reduction C_{LRMS}
Fine-B	1.06	0.097	4.3%	0.15%	61.7%
McClure	1.06	0.012	–	$\approx 2\%$	$\approx 80\%$

Table 3.1.1: Table to represent differences between Fine-B and McClure et al. (2015) for the dual step cylinder with $L/D = 1$ and $D/d = 2$. Each row in order presents the large cylinder $\overline{C_D}$ and C_{LRMS}, and the reduction in $\overline{C_D^*}$, $\overline{C_D}$ and C_{LRMS} compared to the force coefficients of a uniform cylinder with diameter d over the whole dual step cylinder. $Re_D = 150$ for both Fine-B and McClure et al. (2015).

To summarize, the question is why McClure et al. (2015) found the value for C_{LRMS} on the large cylinder to be eight times smaller than the value that

is found in this thesis for a dual step cylinder with the same geometrical parameters. The first observation is that there was less defined shedding in the wake behind the large cylinder in McClure et al. (2015), as seen in figure 3.1.1, compared to the complex vortex loops and vortex interactions in the wake behind the large cylinder in Fine-B, as seen in figure 3.1.2. The second observation is that the vorticity was symmetric and weak in the far wake behind the large cylinder in McClure et al. (2015), as seen in figure 3.1.3, compared to the asymmetric vorticity that is strong in the far wake in Fine-B, as seen in figure 3.1.4. The amplitude of the lift force on the large cylinder will be greatly affected by those two observations as they are the source of the lift force generation. Based on figure 3.1.3 at $(x/D, y/D) = (6, 0.5)$, there is a possibility that the grid refinement in the simulation by McClure et al. (2015) was too coarse and the results could have been smeared by this, leading to different results compared to simulation Fine-B.

In table 3.1.1, there is a 4.3% reduction in $\overline{C_D^*}$ which highlights the difference between calculating $\overline{C_D^*}$ from equation 2.3 and $\overline{C_D}$ from equation 3.3 when comparing the force coefficients of the dual step cylinder to that of a uniform cylinder over the whole span. As seen in table 3.1.1, based on the reduction in $\overline{C_D}$, there is 0.15% reduction in the mean drag coefficient compared to a uniform cylinder when the extra area of the large cylinder part is not accounted for. In reality, this compares the direct forcing on the dual step cylinder to the uniform cylinder over the whole span and finds no reduction in the drag force.

Case Fine-B is based on a simulation time of just $200tU/D$ (after the flow is developed, i.e after the spin up). In chapter 3.3, the analysis of three dual step cylinders with $D/d = 1.33$ and $L/D = 1, 3$ and 5 are simulated with a much longer simulation time of $1200tU/D$. The simulations in table 2.1.1 would have needed to run for a longer time interval to be able to produce reliable results, but the differences in the results between McClure et al. (2015) and simulation Fine-B are qualitative rather than quantitative. They highlight some structural differences even though the results for the time-averaged data in simulation Fine-B has not statistically converged yet.

3.2 Features of the wake flow with varying aspect ratio

The three cases L1, L3 and L5 from table 2.4.1 each presents interesting flow phenomena. To classify the different vortex shedding cells of the dual step cylinder, the frequency content of the vortex shedding along the span is analyzed for the three cases. In figure 3.2.1(a), (b) and (c), the streamwise velocity frequency spectrum for case L1, L3 and L5, respectively, is obtained by means of a Fast Fourier Transform (FFT) of continuous data along a sampling line parallel to the z-axis at position $(x/D, y/D) = (1.6, 0.4)$, over a period of $1000tU/D$.

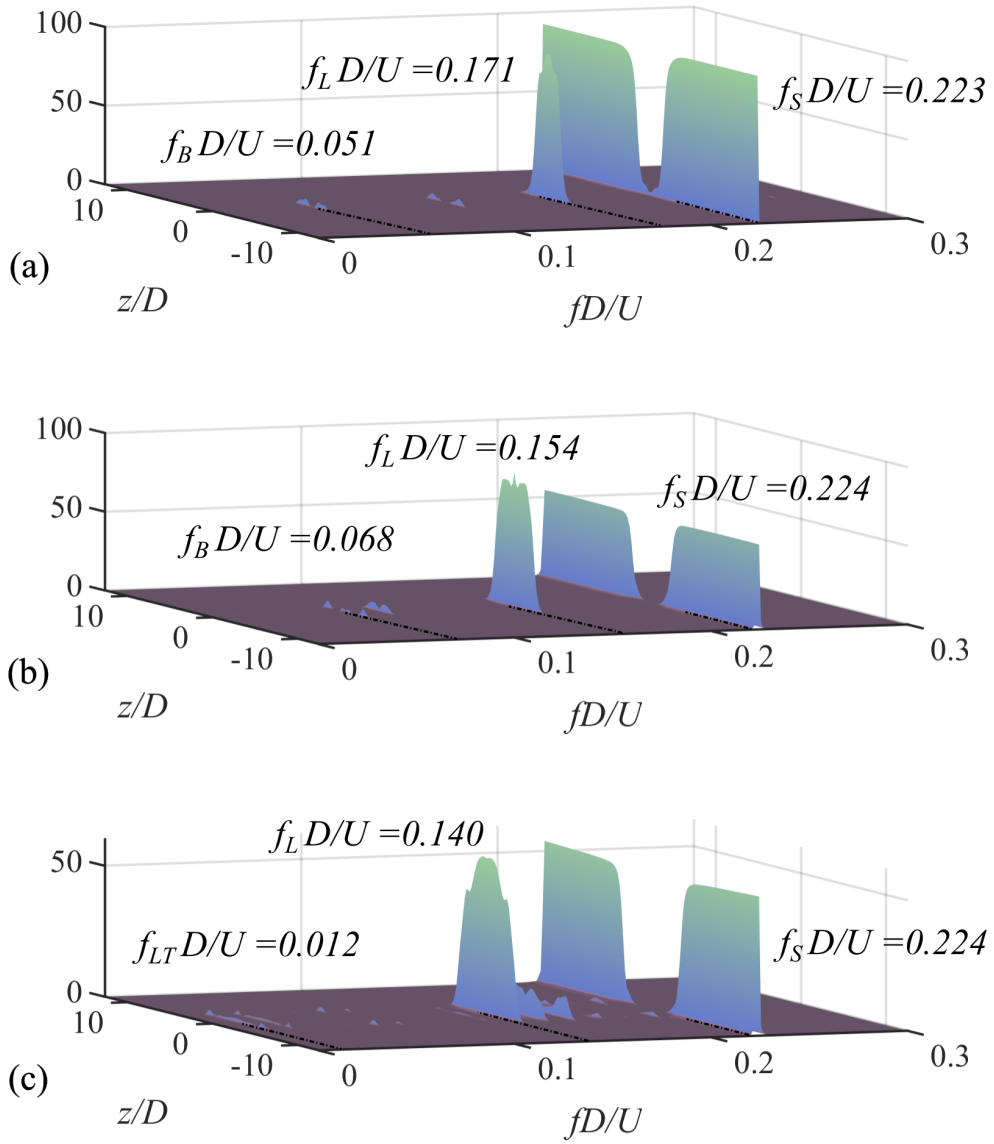

Figure 3.2.1: 3D frequency spectrum plot of the streamwise velocity fluctuations for case L1, L3 and L5 in (a), (b) and (c), respectively. It is obtained by means of a Fast Fourier Transform (FFT) of continuous data along a sampling line parallel to the z-axis at position $(x/D, y/D) = (1.6, 0.4)$, over a period of $1000tU/D$.

Figure 3.2.1 gives insight to the spanwise variation in the vortex shedding frequencies across the wake. There are two dominant frequency peaks observed in all three cases, which are the small cylinder vortex shedding frequency $f_S D/U$ away from the steps in the small cylinder wake, and the large cylinder vortex shedding frequency $f_L D/U$ centered at the mid-span of the large cylinder. In figure 3.2.1(a) and (b) there is also detected a beat frequency, defined as $f_B D/U = f_S D/U - f_L D/U$. As the vortices in the wake behind the large and small cylinders shed at different frequencies, the relative distance between the large cylinder vortex and the small cylinder vortices is growing. The beat frequency $f_B D/U$ is the periodic occurrence when that distance grows too large, triggering a vortex dislocation such that the small cylinder vortices realign and synchronize together across the wake behind the large cylinder. The vortex structures repeats at the periodic occurrence of the beat frequency $f_B D/U$, which can be seen in figure 3.2.2 and 3.2.3 for case L1 and L3 respectively. In figure 3.2.2 for case L1, the vortex structures are captured at $tU/D = 2040$ on the left side of the plot, and on the right, three beat periods later, at $tU/D = 2040 + 3/(f_B D/U) = 2098.8$. In figure 3.2.3 for case L3, the vortex structures are captured at $tU/D = 2115$ on the left side of the plot, and on the right, four beat periods later, at $tU/D = 2115 + 4/(f_B D/U) = 2173.8$. There was not detected a dominant beat frequency $f_B D/U$ for case L5.

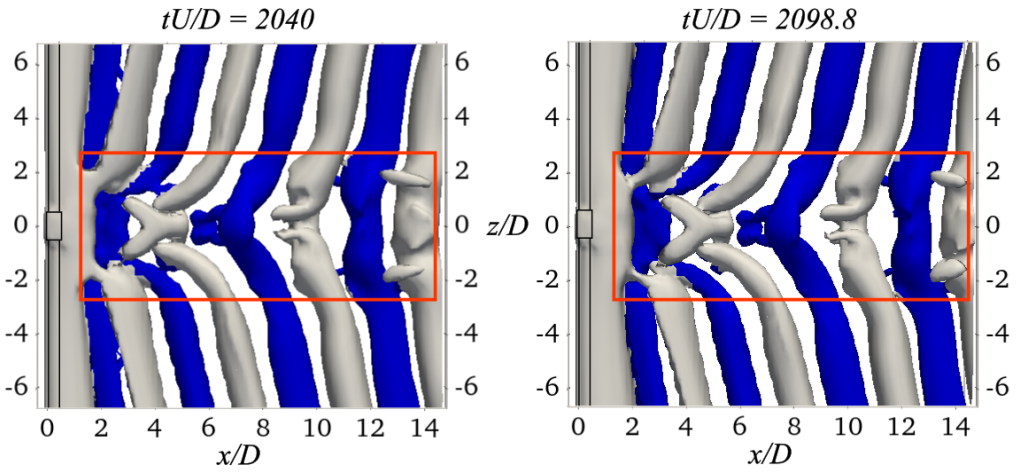

Figure 3.2.2: Instantaneous isosurfaces of $\lambda_2 = -0.01$ for case L1, illustrating how the vortex structures repeat at the beat frequency $f_B D/U$. The structures on the left are captured at $tU/D = 2040$ and on the right, three beat periods later, at $tU/D = 2040 + 3/(f_B D/U) = 2098.8$. The complex vortex structures within the orange rectangle can be seen to repeat at the beat frequency $f_B D/U$. The color of the isosurfaces represent the sign of the z-component of the vorticity.

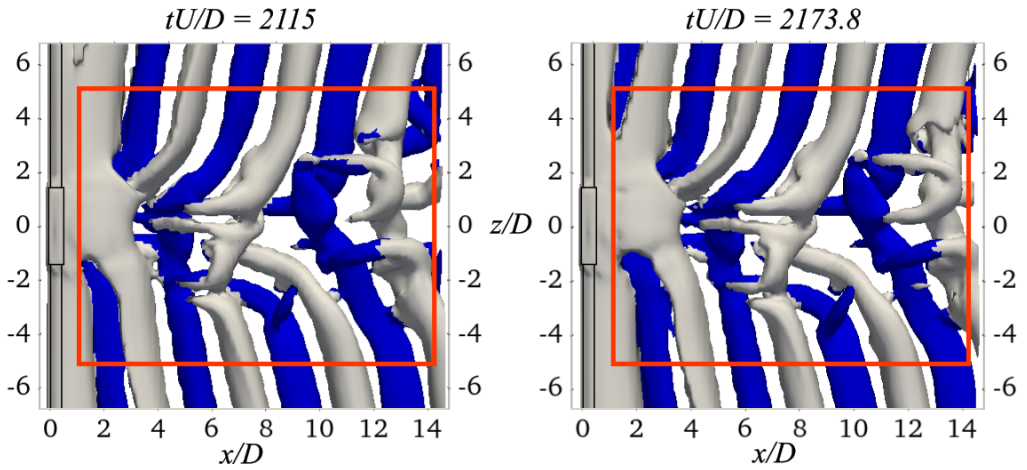

Figure 3.2.3: Instantaneous isosurfaces of $\lambda_2 = -0.01$ for case L3, illustrating how the vortex structures repeat at the beat frequency $f_B D/U$. The structures on the left are captured at $tU/D = 2115$ and on the right, four beat periods later, at $tU/D = 2115 + 4/(f_B D/U) = 2173.8$. The complex vortex structures within the orange rectangle can be seen to repeat at the beat frequency $f_B D/U$. The color of the isosurfaces represent the sign of the z-component of the vorticity.

In the wake behind the large cylinder for case L5, there are at least two other secondary vortex shedding frequencies that are detected in addition to the large cylinder shedding frequency $f_L D/U$, and can be seen in figure 3.2.1(c), where there are two peaks of slightly higher frequency behind the $f_L D/U$ peak. The reason for this phenomena is unknown in this thesis, but it is possible that there is a co-existence of an N-cell, which was introduced in chapter 1, and an L-cell that interchange. What is certain is that there is a dominant shedding frequency in the wake behind the large cylinder, being $f_L D/U$.

For all cases in figure 3.2.1, there is a gradual transition across the steps where both the magnitude of the large cylinder frequency $f_L D/U$ and the magnitude of the small cylinder frequency $f_S D/U$ is decreased, leading to a region near the step where there is frequency content of both the large- and small cylinder present. This is the region where the complex vortex interactions initiate, like the ones seen within the orange rectangles in figure 3.2.2 and 3.2.3. In this thesis, there was not observed any fundamental dislocation frequencies. This is due to the fact that the small cylinders shed vortices either perfectly in phase or perfectly out of phase (180°), leading to no long-term correction of phase difference between the small cylinder vortices. As the aspect ratio increases, there is only a minute difference in the small cylinder frequencies $f_S D/U$ with $f_S D/U = 0.223$, 0.224 and 0.224 for case L1, L3 and L5, respectively. But the large cylinder frequencies $f_L D/U$ decrease as the aspect ratio increases with $f_L D/U = 0.171$, 0.154 and 0.140 for case L1, L3 and L5, respectively. This is the same trend that was observed in McClure et al. (2015). When the aspect ratio increases, the large cylinder vortices grow larger and stronger and are less affected by the shedding frequency of the small cylinder vortices.

In figure 3.2.4(a) and (b), the vortex structures of case L1 and L5, respectively, are shown. The solid lines that cover the entire span of the dual step cylinder highlight where there is a direct connection between the small cylinder vortices across the wake behind the large cylinder, and the dotted lines show how the various vortex filaments and half-loops connect.

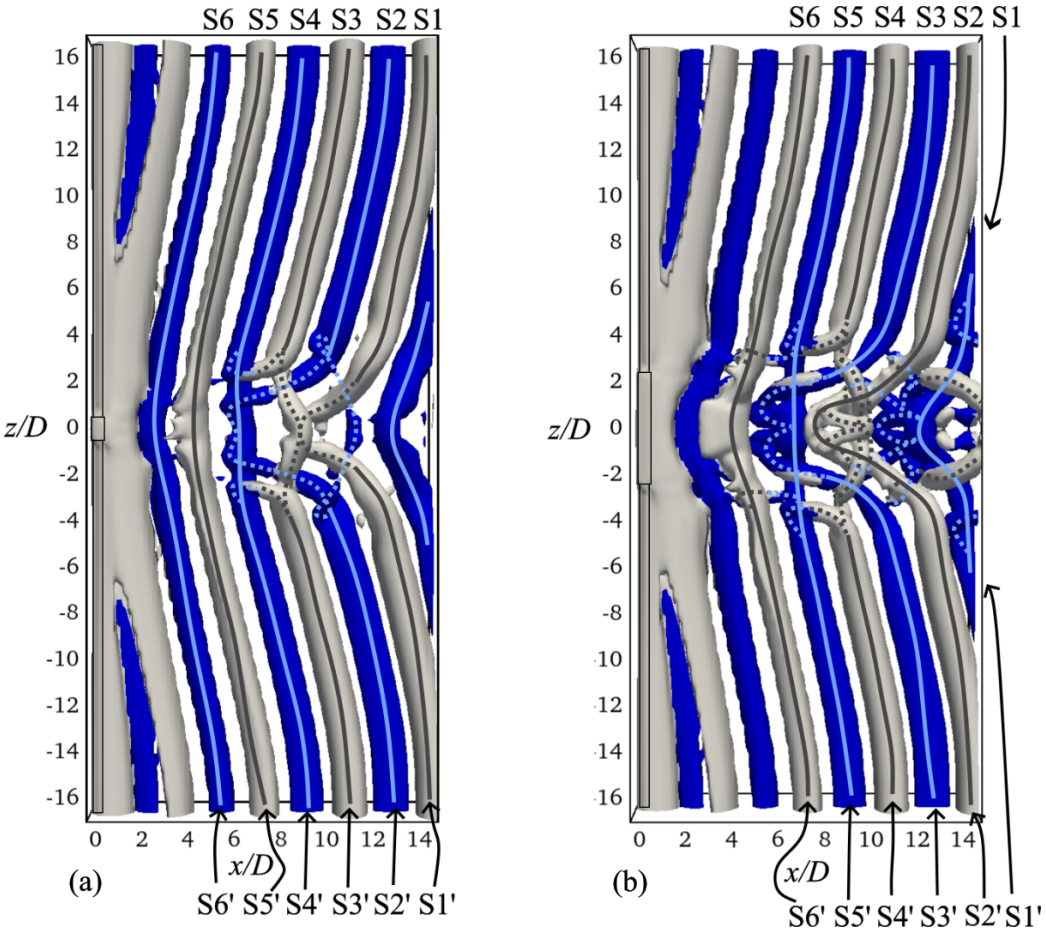

Figure 3.2.4: Instantaneous isosurfaces of $\lambda_2 = -0.01$ for case L1 at $tU/D = 2086.8$ in (a) and case $L5$ at $tU/D = 2126.9$ in (b). The color of the isosurfaces represent the sign of the z-component of the vorticity. Lines visualize the vortices, where the dotted lines visualize where vortex filaments and half-loops connect. Where there is a solid line drawn from top to bottom, there is a direct connection between the small cylinder vortices across the wake behind the large cylinder.

For case L1 in figure 3.2.4(a), the aspect ratio $L/D = 1$ is very narrow. The large cylinder vortices, that were detected in figure 3.2.1(a), are shedding, but do not seem to be acting as a strong distinct bridge to connect the small cylinder vortices across the wake behind the large cylinder. The small cylinder vortices seem to have enough strength in comparison, to be able to conjoin with the large cylinder vortices and connect with each other across the wake behind the large cylinder. The large cylinder vortices reduce the convective velocity of the small cylinder vortices that connect across the wake behind the large cylinder. This is similar to the observations of McClure et al. (2015). As the relative distance between the vortices in the wake behind the large

cylinder and the small cylinder vortices grows, a realignment occurs where the direct connection across the wake behind the large cylinder is broken and replaced by complex vortex interactions near the step wakes with different vortex filaments connecting to surrounding vortices. This complex vortex interaction is then followed by a synchronization of the small cylinder vortices when they once again realign and directly connect across the wake behind the large cylinder in phase with each other. This synchronization, caused by the direct connection across the wake behind the large cylinder, can be seen in figure 3.2.4(a) where the small cylinder vortices $S4$ and $S4'$ connect with each other across the wake behind the large cylinder after the vortices $S1$, $S2$ and $S3$ were unable to directly connect to their counterparts $S1'$, $S2'$ and $S3'$. The relative distance that had grown before the realignment can be seen in figure 3.2.4(a) at $(x/D, z/D) \approx (14, 0)$ where the vortices are still directly connected, but the part in the wake behind the large cylinder lags behind the small cylinder vortices that connect to it. The realignment in figure 3.2.4(a) between vortices $S4$ and $S4'$ is happening at the beat frequency $f_B D/U$.

In case L5 there are vortices shedding from the large cylinder, as was detected in figure 3.2.1(c). The large cylinder vortices appear to be strong and defined enough such that the small cylinder vortices are not able to conjoin together, but rather connect to both sides of the large cylinder vortices to connect across the wake behind the large cylinder. Due to the difference in convective speed of the large- and small cylinder vortices, like for case L1, the relative distance between the small- and large cylinder vortices grows until the direct connection across the wake behind the large cylinder is broken. Contrary to L1, the presence of the more defined large cylinder vortices gives an even larger and more complex vortex deformation, with multiple vortex filaments from the large cylinder vortex connecting to nearby small- and large cylinder vortices. This can be seen in figure 3.2.4(b), where vortex $S2$ and $S2'$ are barely connected across the wake behind the large cylinder, but with a huge relative difference amassed. The successive vortices $S3$ and $S3'$ do not connect across the wake behind the large cylinder, but are rather pulled towards the large cylinder vortex that conjoins vortex $S5$ and $S5'$ and is connecting to it via weaker vortex filaments, which can be seen at $(x/D, z/D) \approx (6, 0)$. Vortices $S4$ and $S4'$ do not connect across the wake behind the large cylinder as well, but rather connect to both $S2/S2'$ and $S5/S5'$ via multiple vortex filaments, highlighting the complexity of the vortex structures in case L5. A synchronization of the small cylinder vortices is achieved with the connection of vortices $S5$ and $S5'$ across the wake behind the large cylinder, which also leaves the small cylinder vortices synchronized in phase.

In figure 3.2.5, the vortex structures of case L3 are shown. In case L3, the vortex structures in the wake behind the large cylinder are heavily deformed and consists of complicated vortex filaments from multiple small cylinder vortices. There are vortices shedding from the large cylinder, that were detected in figure 3.2.1(b), but unlike case L5, the large cylinder vortices do not seem to be defined enough such that the small cylinder vortices can connect to both sides of them to connect across the wake behind the large cylinder.

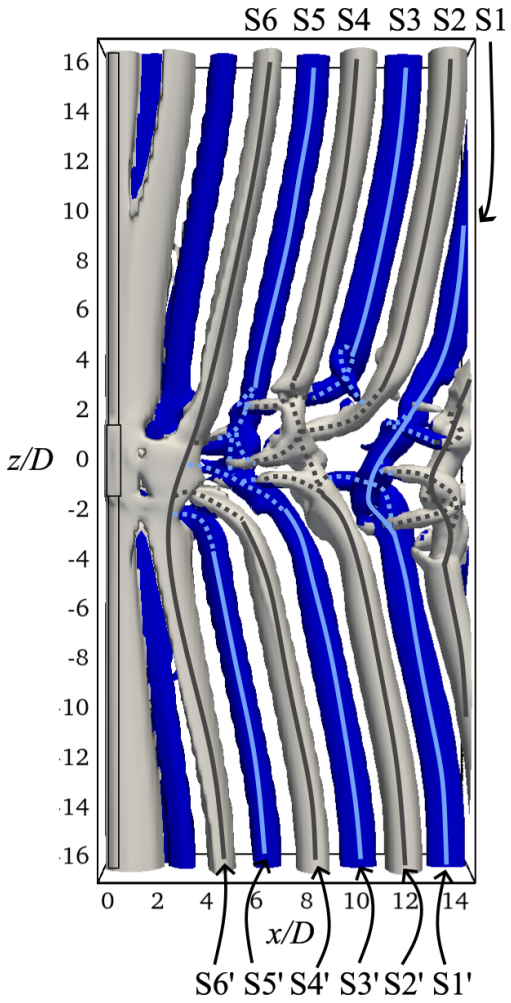

Figure 3.2.5: Instantaneous isosurfaces of $\lambda_2 = -0.01$ for case L3 at $tU/D = 2109$. The color of the isosurfaces represent the sign of the z-component of the vorticity. Lines visualize the vortices, where the dotted lines visualize where vortex filaments and half-loops connect. Where there is a solid line drawn from top to bottom, there is a direct connection between the small cylinder vortices across the wake behind the large cylinder.

Also, unlike case L1, the large cylinder vortices are still strong enough such that the small cylinder vortices are not able to conjoin with them and connect with each other across the wake behind the large cylinder. Whenever there is a direct connection between the small cylinder vortices across the wake behind the large cylinder for case L3, the connection is heavily deformed and does not constitute a strong bridge for the small cylinder vortices. This weak connection can be seen in figure 3.2.5 between small cylinder vortices $S1$ and $S1'$, which also connect to the neighbouring vortices by vortex filaments, dissipating energy from the connection. The aspect ratio $L/D = 3$ for case L3 seems to be in a transition state where the small cylinder vortices are not able to conjoin with the large cylinder vortices and connect with each other across the wake behind the large cylinder, due to the large cylinder shedding being too strong. On the other hand, the small cylinder vortices are also not able to connect to both sides of the large cylinder vortices to connect across

the wake behind the large cylinder, due to the large cylinder shedding being too weak to create a strong defined bridge. As there is no strong connection between the two small cylinders, the realignment and synchronization that is observed in case L1 and L5 does not happen for case L3, and the small cylinder vortices end up shedding relatively independently of each other. Because of this independent shedding, case L3 eventually obtains a stable state where the small cylinder vortices shed completely 180° out of phase to each other. Looking at figure 3.2.5, we can see the complex vortex interactions that happens due to the vortices being out of phase. The small cylinder vortex $S3$ does not connect to its counterpart $S3'$, but rather forms a half-loop with $S4$, which can be seen at $(x/D, z/D) \approx (8.5, 3)$, in addition to a small vortex filament connecting to $S2$. Small cylinder vortex $S3'$, on the other hand, connects to $S5$. There is also a complex vortex interaction between small cylinder vortices $S2$, $S4$ and $S2'$ that forms a very deformed connection in the wake behind the large cylinder that also connects to the large cylinder wake section of the $S5/S3'$ vortex via multiple vortex filaments. This can be seen at $(x/D, z/D) \approx (7, 0)$.

3.3 Effects on structural loading with varying aspect ratio

This section will investigate how the features of the wake flow affects the structural loading on the dual step cylinders with varying aspect ratios. In figure 3.3.1, the time series of the lift force F_L and the drag force F_D at $1400 \leq tU/D \leq 2200$ for cases L1, L3 and L5 are shown.

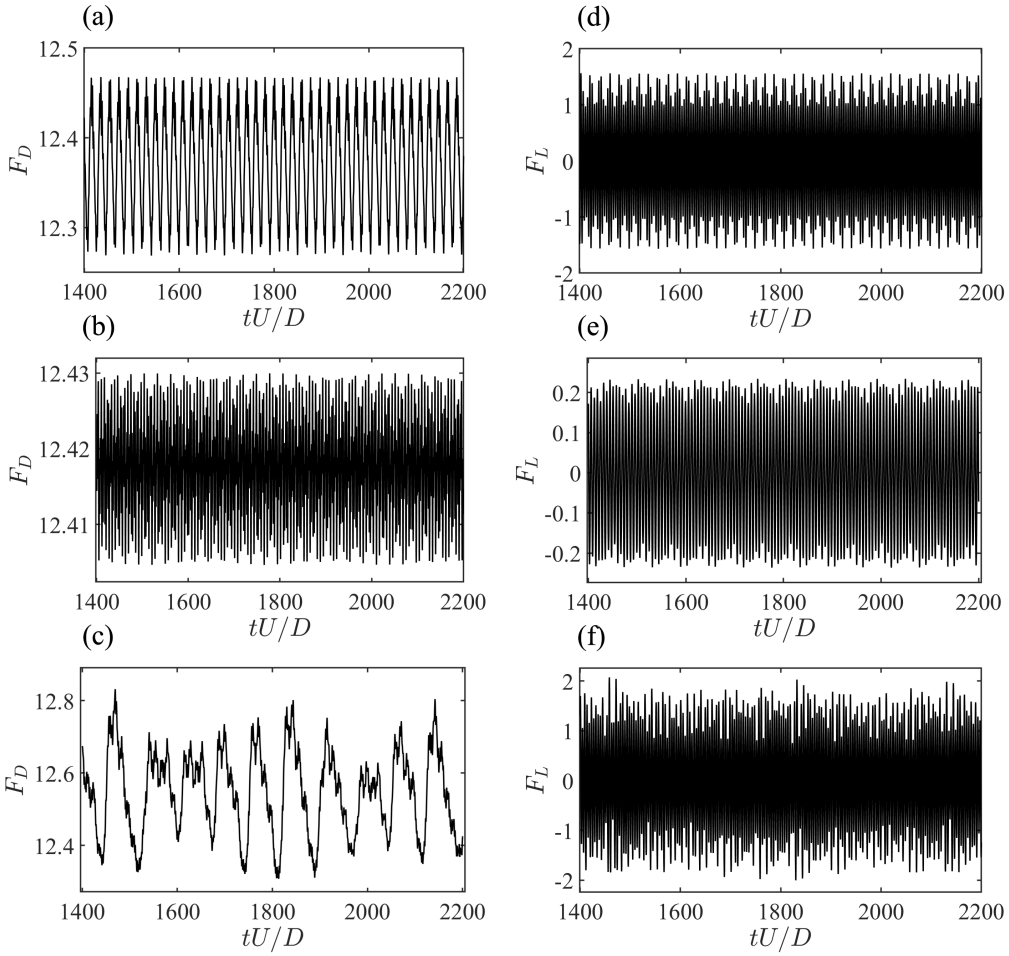

Figure 3.3.1: Time series of the lift force F_L and the drag force F_D at $1400 \leq tU/D \leq 2200$ for cases L1, L3 and L5. F_D for cases L1, L3 and L5 is shown in (a), (b) and (c), respectively. F_L for cases L1, L3 and L5 is shown in (d), (e) and (f), respectively.

Based on figure 3.3.1, it is clear that the wake flow is fully developed in all cases, as there is no major variation in the amplitude of the forces and there is no variation in the mean. All the force-plots in figure 3.3.1, except from (c), mainly consists of the small cylinder frequency $f_S D/U$ with a high amplitude, in addition to other low-amplitude lower frequency components, such as the large cylinder frequency $f_L D/U$ and the beat frequency $f_B D/U$, that give the forces different longer periodic variations. The 3D frequency spectrum plot of the streamwise velocity fluctuations for cases L1, L3 and L5 is found in figure 3.2.1.

In figure 3.3.1(c), the drag force is different to the other force-plots in figure 3.3.1. The frequency spectrum in figure 3.2.1(c) for case L5 is more complex and contains a broader range of frequency content than case L1 and L3. There is also another dominant frequency peak in figure 3.2.1(c) for case L5, which is the quasi-periodic very low frequency $f_{LT}D/U$. This is the same peak as we can see in figure 3.3.2, which is the frequency content of the time history of the drag force F_D. Therefore, the long term shedding frequency $f_{LT}D/U = 0.012$ could then be said to influence the time series of the drag force for case L5 in figure 3.3.1(c), giving it the large amplitude, quasi-periodic long-term variation.

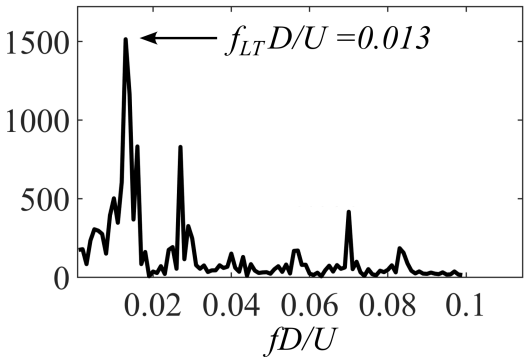

Figure 3.3.2: Frequency content of the time history of the drag force F_D for case L5. It is obtained by means of a Fast Fourier Transform (FFT) of the time history of the drag force F_D, over a period of $1000tU/D$.

In figure 3.3.1(e), the fluctuating lift force F_L is presented for case L3. The rms value of F_L for case L3 is 0.148. Compared to the rms value of the fluctuating lift forces from case L1 and L5, which is 0.90 and 1.03, respectively, case L3 has an approximately 6.5 times smaller value. In figure 3.3.3, the time series of the lift force in case L3 is presented at $400 \leq tU/D \leq 800$.

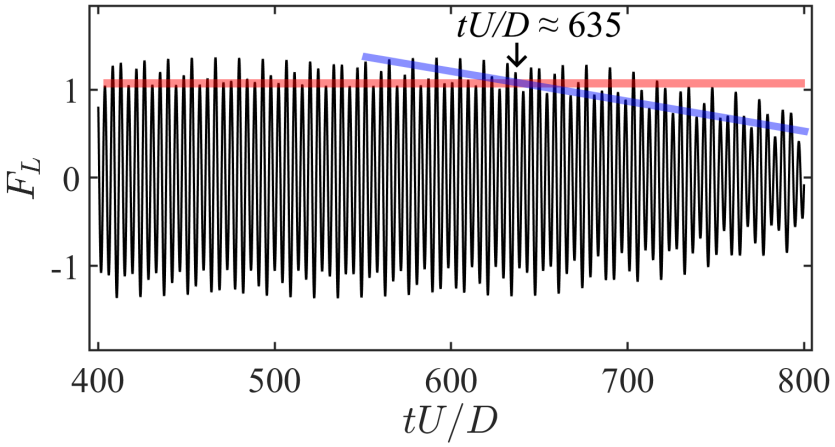

Figure 3.3.3: Time series of the lift force F_L for case L3 at $400 \leq tU/D \leq 800$. At $tU/D \approx 635$, the amplitude begins to decrease, due to an increasing phase difference between the small cylinder vortices.

There seems to be an instability that triggers at $tU/D \approx 635$, which causes the small cylinder vortices to steadily begin to go out of phase of each other. Before that point, the small cylinder vortices in case L3 were synchronized and were shedding in phase with each other. The fluctuating lift force is caused by the vortex shedding on the small cylinders predominantly. There-

fore, when the small cylinder vortices starts to move out of phase, then the lift forces that are generated on both the small cylinders begin to cancel each other out. There is only cancellation of forces if the lift force is measured on the dual step cylinder as a whole, meaning a combination of the forces both above and below the large cylinder part. As discussed in section 3.2, the state in which case L3 stabilizes in is a state where the small cylinder vortices are shedding completely out of phase (180°). This is the reason for a 6.5 times smaller value for the rms lift force in case L3, compared to case L1 and L5. The small cylinder vortices shed on opposite sides of the cylinder in each cycle, leading to a cancellation of the fluctuating lift force.

After analyzing how the features of the wake flow affects the structural loading on the dual step cylinders with varying aspect ratios, the total structural loading of cases L1, L3 and L5 is to be calculated and compared against the structural loading of a uniform cylinder. This is to understand the effects of attaching a cylinder of a larger diameter to the mid-span of a uniform cylinder. As the drag- and lift forces are measured on N spanwise locations along the span of the dual step cylinder, equations 3.1 and 3.2 sum them up to express the time series of the drag force F_D and the lift force F_L of the whole cylinder span. This is the way McClure et al. (2015) calculated the total structural loading.

$$F_D(t) = \sum_{i=1}^{N} F_{D,i}(t) \tag{3.1}$$

$$F_L(t) = \sum_{i=1}^{N} F_{L,i}(t) \tag{3.2}$$

The formulas that are used to calculate the force coefficients the mean drag $\overline{C_D}$ and the rms lift C_{LRMS} are

$$\overline{C_D} = \frac{1}{T} \sum_{t=1}^{T} \frac{2F_D(t)}{\rho U^2 A} \tag{3.3}$$

$$C_{LRMS} = \sqrt{\frac{1}{T} \sum_{t=1}^{T} (C_L(t) - \overline{C_L})^2} \tag{3.4}$$

$$C_L(t) = \frac{2F_L(t)}{\rho U^2 A} \tag{3.5}$$

$$\overline{C_L} = \frac{1}{T} \sum_{t=1}^{T} C_L(t) \tag{3.6}$$

where ρ is the water density, U the velocity of the incoming flow, $F_D(t)$ the time series of the drag force defined in equation 3.1 and $F_L(t)$ the time series of the lift force defined in equation 3.2. As the forces are compared to a uniform cylinder, the two-dimensional area that is used in equation 3.3 and 3.5 is $A = 2ld + Ld$, which is the area of an unmodified uniform cylinder

of length $2l + L$ and diameter d. There was a simulation conducted of a uniform cylinder at $Re_d = 112.5$, and the calculated force coefficients were $\overline{C_D} = 1.309$ and $C_{LRMS} = 0.265$. In figure 3.3.4, the mean drag $\overline{C_D}$ and the rms lift C_{LRMS} are normalized with the corresponding force coefficients of the uniform cylinder. To evaluate the significance of the vortices shedding out of phase, the phase corrected force coefficients were calculated by isolating the forces above and below $z/D = 0$ and calculate the force coefficients, before combining them together. The phase corrected force coefficients are calculated for all points in figure 3.3.4, but for all values except for C_{LRMS} in case L3, there is no difference. McClure et al. (2015) investigated a dual step cylinder with $L/D = 5$ and $D/d = 1.33$, just like case L5, and the resulting force coefficients are presented in figure 14(b) in McClure et al. (2015). Those force coefficients are also presented in figure 3.3.4.

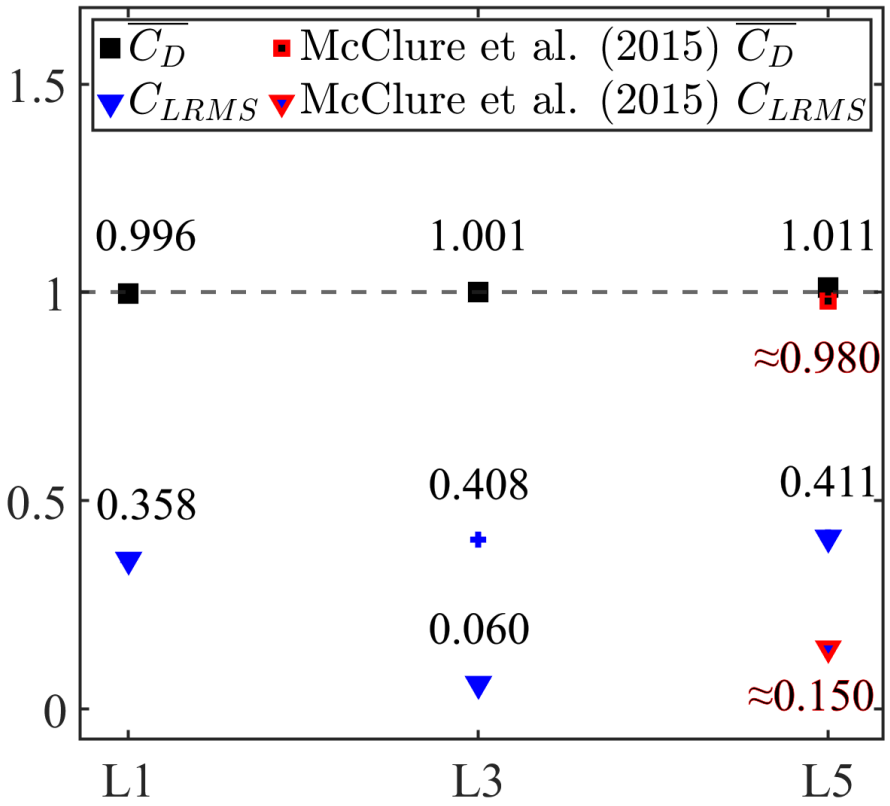

Figure 3.3.4: The mean drag $\overline{C_D}$ (■), rms lift C_{LRMS} (▼) and phase corrected C_{LRMS} (✚) for cases L1, L3 and L5, normalized by force coefficients of a uniform cylinder. The dotted line indicates the force coefficients of a uniform cylinder at $Re_d = 112.5$. The points with a red border are the results from figure 14(b) in McClure et al. (2015) for a dual step cylinder with the same dimensions as case L5.

The results from figure 3.3.4 show that there is a tiny, but steady, increase in $\overline{C_D}$ as the aspect ratio increases, and that there is virtually no difference in $\overline{C_D}$ on a uniform cylinder compared to a dual step cylinder with the

aspect ratios studied in this thesis at $Re_D = 150$. There is a reduction in C_{LRMS} on a dual step cylinder compared to a uniform cylinder. Due to the asynchronous shedding in the stable out-of-phase regime of case L3, there is a 94% reduction in C_{LRMS} across the whole dual step cylinder length for case L3 compared to a uniform cylinder. For the aspect ratios L1 and L5, there is a 64% and 59% reduction, respectively, in C_{LRMS} compared to a uniform cylinder. For case L5, there is a substantial difference in the values McClure et al. (2015) achieves for the non-phase corrected lift. McClure et al. (2015) achieves $\approx 85\%$ reduction in C_{LRMS} while in this thesis there is found a 59% reduction. Although for the phase corrected reduction in C_{LRMS}, McClure et al. (2015) achieves only 54% reduction compared to the 59% reduction found in this thesis. There is a 2% difference in the reduction in $\overline{C_D}$ between McClure et al. (2015) and the findings of this thesis. Based on the findings in figure 3.3.4, the addition of the large cylinder part to a uniform cylinder has virtually no effect in reducing the drag force, but it can reduce the lift force by up to 96%.

CHAPTER 4

Summary and conclusion

The main motivation for the topic of this thesis was that McClure et al. (2015) investigated a dual step cylinder with diameter ratio $D/d = 1.33$ and aspect ratio $L/D = 5$ at $Re_D = 150$. Here there was an $\approx 85\%$ reduction in the non-phase corrected rms lift C_{LRMS}, and for dual step cylinders with smaller aspect ratios there was up to 5% reduction in the mean drag $\overline{C_D}$. A direct comparison was conducted in this thesis for a dual step cylinder with $D/d = 2$ and $L/D = 1$ at $Re_D = 150$, where there was found a substantial difference in the C_{LRMS} value on the large cylinder part in this thesis, compared to the results in McClure et al. (2015). The reasons for this are not clear, however a consistent grid refinement, keeping the CFL number smaller than 0.5, are underpinning the results of this thesis.

A dual step cylinder with $D/d = 1.33$ achieved the best reduction in C_{LRMS} compared to the forcing on a uniform cylinder in McClure et al. (2015), but there was not conducted an aspect ratio study with this diameter ratio in McClure et al. (2015). Rather, they conducted an aspect ratio study of a dual step cylinder with $D/d = 2$. This thesis studied three dual step cylinders with $D/d = 1.33$ and $L/D = 1, 3$ and 5 and analyzed how changing the aspect ratio affects the wake topology and the structural loading. As L/D is increased from 1 to 5, there is a big change in the wake topology. For $L/D = 1$, the small cylinder vortices conjoin with the large cylinder vortex and connect together across the wake behind the large cylinder. For $L/D = 5$, the small cylinder vortices connect to both sides of the large cylinder vortex to connect across the wake behind the large cylinder. For $L/D = 3$, there seems to be a transition regime where the small cylinder vortices are unable to form a strong connection across the wake behind the large cylinder in order to synchronize their shedding. The small cylinder vortices for $L/D = 3$ end up shedding relatively independent and stabilizes in a state where they shed completely ($180°$) out of phase. The lift force is greatly affected by the small cylinder vortices shedding out of phase, as the forces begin to cancel each other out when they are acting in opposite

directions, and there is a 94% reduction in C_{LRMS} on the dual step cylinder compared to the forcing on a uniform cylinder due to this phenomena. The mean drag $\overline{C_D}$ is steadily increasing with L/D, and there is not found any reduction in $\overline{C_D}$ compared to the forcing on a uniform cylinder. The phase corrected C_{LRMS} is also steadily increasing with L/D in this thesis, so there is no optimal geometrical configuration found based on this study that minimizes the phase corrected structural loading. If the phenomena of the asynchronous shedding is reproducible, then $L/D = 3$ presents the optimal geometrical configuration for a dual step cylinder with $D/d = 1.33$ in laminar flow at $Re_D = 150$.

For a dual step cylinder with $D/d = 1.33$ and $L/D = 5$, McClure et al. (2015) found that the small cylinder vortices were shedding at a phase difference, leading to a non-phase corrected reduction in C_{LRMS} of $\approx 85\%$ and a phase corrected reduction in C_{LRMS} of $\approx 54\%$ compared to the forcing on a uniform cylinder. This thesis achieved the same phase corrected and non-phase corrected reduction in C_{LRMS} for a dual step cylinder with $D/d = 1.33$ and $L/D = 5$ at 59% compared to the forcing on a uniform cylinder. This was a 5% better reduction in the phase corrected C_{LRMS}, in comparison to the results in McClure et al. (2015). As for the mean drag $\overline{C_D}$, McClure et al. (2015) finds an $\approx 2\%$ reduction compared to the forcing on a uniform cylinder for a dual step cylinder with $D/d = 1.33$ and $L/D = 5$, whereas this thesis finds no reduction.

4.1 Further work

Additional simulations of dual step cylinders with $D/d = 1.33$ and aspect ratio closer to $L/D = 3$ would give great insight into the phenomena of the asynchronous shedding discovered in this thesis. There is a chance that this was an isolated instance, and a slight difference to the geometry might induce the dual step cylinder to shed in phase like case L1 and L5. In that case, where a dual step cylinder with a similar aspect ratio to L3 is shedding in phase, the value for C_{LRMS} would likely be close to the value of the phase corrected C_{LRMS} for case L3. In that scenario, figure 3.3.4 shows that there is an increase in C_{LRMS} with an increasing L/D. Since the best reduction in the phase corrected C_{LRMS} is 64% for case L1 compared to the forcing on a uniform cylinder, additional simulations of dual step cylinders with $D/d = 1.33$ and $L/D < 1$ would give insight into whether the optimal L/D for reduction in the force coefficients compared to a uniform cylinder is less than $L/D = 1$.

Another interesting phenomena that could be further investigated is the secondary frequency components that are present in the wake behind the large cylinder in case L5. This can be seen in figure 3.2.1(c). There is a possibility of a co-existence of an N-cell and an L-cell in the wake behind the large cylinder. Another interest from case L5 is the long term frequency component $f_{LT}D/U$ that is identified in figure 3.2.1(c) and 3.3.2, which could be further investigated to find the cause for this quasi-periodic long term frequency.

References

Bearman, P. W., & Owen, J. C. (1998). Reduction of bluff-body drag and suppression of vortex shedding by the introduction of wavy separation lines. *Journal of Fluids and Structures*, *12 (1)*, 123–130.

Dunn, W., & Tavoularis, S. (2006). Experimental studies of vortices shed from cylinders with a step-change in diameter. *Journal of Fluid Mechanics*, *555*, 409–437.

Ji, C., Yang, X., Yu, Y., Cui, Y., & Srinil, N. (2020). Numerical simulations of flows around a dual step cylinder with different diameter ratios at low reynolds number. *European Journal of Mechanics B-fluids*, *79*, 332–344.

Jiang, F., Pettersen, B., Andersson, H. I., Kim, J., & Kim, S. (2018). Wake behind a concave curved cylinder. *Physical Review Fluids*, *27 (9)*, 063602.

Lee, S., & Nguyen, A.-T. (2007). Experimental investigation on wake behind a wavy cylinder having sinusoidal cross-sectional area variation. *Fluid Dynamics Research*, *39 (4)*, 292–304.

Manhart, M. T. (2004). A zonal grid algorithm for dns of turbulent boundary layers. *Computers & Fluids*, *33*, 435–461.

McClure, J., Morton, C., & Yarusevych, S. (2015). Flow development and structural loading on dual step cylinders in laminar shedding regime. *Physics of Fluids*, *27*, 063602.

Morton, C., & Yarusevych, S. (2020). Vortex shedding from cylinders with two step discontinuities in diameter. *Journal of Fluid Mechanics*, *902, A29*.

Nakamura, H., & Igarashi, T. (2008). Omnidirectional reductions in drag and fluctuating forces for a circular cylinder by attaching rings. *Journal of Wind Engineering and Industrial Aerodynamics*, *96 (6-7)*, 887–899.

Owen, J. C., Bearman, P. W., & Szewczyk, A. A. (2001). Passive control of viv with drag reduction. *Journal of Fluids and Structures*, *15 (3-4)*, 597–605.

Peller, N., Duc, A. L., Tremblay, F., & Manhart, M. T. (2006). High-order stable interpolations for immersed boundary methods. *International Journal for Numerical Methods in Fluids*, *52 (11)*, 1175–1193.

Stone, H. L. (1968). Iterative solution of implicit approximations of multidimensional partial differential equations. *SIAM Journal on Numerical Analysis*, *5*, 530–558.

Sumer, B. M., & Fredsøe, J. (2006). *Hydrodynamics around cylindrical structures*. World Scientific Publishing Co. Pte. Ltd.

Tian, C., Jiang, F., Pettersen, B., & Andersson, H. I. (2020). Vortex dislocation mechanisms in the near wake of a step cylinder. *Journal of Fluid Mechanics*, *891*.

Tian, C., Zhu, J., & Holmedal, L. E. (2022). Flow around i-shape step cylinders.

Tian, C., Zhu, J., & Holmedal, L. E. (2023a). Coexistence of natural and forced vortex dislocations in step cylinder flow. *Physics of Fluids*, *35 (9)*, 094111.

Tian, C., Zhu, J., Holmedal, L. E., Andersson, H. I., Jiang, F., & Pettersen, B. (2023b). How vortex dynamics affects the structural load in step cylinder flow. *Journal of Fluid Mechanics*, *972*.

Williamson, C. H. K. (1996). Vortex dynamics in the cylinder wake. *Annual Review of Fluid Mechanics*, *28*, 477–539.

Williamson, J. H. (1980). Low-storage runge-kutta schemes. *Journal of Computational Physics*, *35*, 48–56.

Wu, J., Lekkala, M. R., & Ong, M. C. (2020). Numerical investigation of vortex-induced vibrations of a flexible riser with staggered buoyancy elements. *Applied Sciences*.

Yin, D., Lie, H., & Wu, J. (2020). Structural and hydrodynamic aspects of steel lazy wave riser in deepwater. *Journal of Offshore Mechanics and Arctic Engineering-transactions of The Asme*, *142 (2)*.

Yoon, H. S., Kim, M. I., & Kim, H. J. (2019). Reynolds number effects on the flow over a twisted cylinder. *Physics of Fluids*, *31 (2)*.

Zhu, J., Tian, C., & Holmedal, L. E. (2024). Flow over a single dimple recessed in a flat plate. *Physics of Fluids*, *36 (2)*, 023608.